Pore-Structure Analysis by Using Nitrogen Sorption and Mercury Intrusion Data

Christos D. Tsakiroglou and Vasilis N. Burganos
Institute of Chemical Engineering and High Temperature Chemical Processes—Foundation for Research and Technology Hellas (FORTH/ICE-HT), Stadiou St., Platani, GR-26504 Patras, Greece

Joachim Jacobsen
Haldor Topsoe A/S, Dept. of Fundamental Research, Nymollevej 55, DK-2800 Lyngby, Denmark

A multistep methodology is developed for the characterization of the pore structure of mesoporous materials from experimental data of mercury intrusion and nitrogen adsorption/desorption. The pore-space geometry is described by the pore- and throat-size distributions and pore-shape factors, while the pore-network topology (connectivity) and spatial pore-size correlations are embedded in suitably selected accessibility functions. Analytical mathematical models of the relevant processes are integrated into numerical codes, developed in the environment of a commercial software package of nonlinear parameter estimation. The methodology is evaluated and calibrated with respect to the well-known parameter values of "theoretical" test materials, and is subsequently applied to the characterization of the pore structure of four samples of porous alumina. *AIChE J,* 50: 489–510, 2004
Keywords: nitrogen sorption, mercury porosimetry, parameter estimation, percolation model, porous media

Introduction

Mercury porosimetry and nitrogen sorption are the most popular experimental techniques used for the analysis of the structure of porous materials. In industrial practice, the interpretation of experimental data is based on the tube-bundle model and the differentiation of the N_2 adsorption/desorption isotherms (Broekhoff and deBoer, 1967, 1968; Bodor et al., 1970), and/or Hg porosimetry curves (Spitzer, 1981; Moscou and Lub, 1981; Smithwick, 1982). In this manner, different techniques may produce different "pore-size distributions" for the same material (de Wit and Scholten, 1975).

In the past, several researchers used concepts of percolation theory and pore network simulations for the interpretation of N_2 sorption isotherms (Mason, 1982, 1983, 1988; Seaton, 1991; Liu et al., 1992, 1993) and capillary pressure curves (Larson and Morrow, 1981; Chatzis and Dullien, 1985; Li et al., 1986; Renault, 1988; Yanuka, 1989a,b; Ioannidis and Chatzis, 1993a; Tsakiroglou and Payatakes, 1990, 1991a,b, 1993; Matthews et al., 1995). Nevertheless, little attention has been paid on the characterization of the structure of mesoporous materials, in terms of pore network models, by deconvolving simultaneously the N_2 adsorption/desorption isotherms and Hg intrusion/retraction curves and producing only one set of geometrical and topological parameters. For example, data from N_2 adsorption and NMR were taken into account for by the interpretation of Hg porosimetry data of catalysts in terms of the parameters of a multiscale pore structure model (Rigby, 2000). NMR images were employed to identify heterogeneities in voidage and pore sizes over a broad range of length scales (Gladden et al., 1995), whereas the use of multiscale pore networks was proved very efficient in the interpretation of Hg porosimetry data for materials exhibiting a broad pore-size distribution (Tsakiroglou and Payatakes, 1993; Xu et al., 1997).

Correspondence concerning this article should be addressed to C. D. Tsakiroglou at ctsakir@iceht.forth.gr.

The assignment of sizes to sites and bonds of a network can be done completely at random so that no correlation exist among the sizes of chambers and those of neighboring throats (uncorrelated networks). When this assignment is done nonrandomly and according to predefined rules concerning the sizes of adjacent pores (for instance, large throats are positioned between large chambers), spatially correlated pore networks are obtained (Tsakiroglou and Payatakes, 1991a; Renault, 1991; Ioannidis et al., 1993b; Matthews et al., 1995).

Simulations of N_2 condensation/evaporation or Hg intrusion/retraction in pore networks enable us to understand the effects of microstructural parameters of the pore space on the shape of the corresponding cumulative curves, by taking into account all significant pore-scale mechanisms of fluid transport (Lapidus et al., 1985; Diaz et al., 1987; Tsakiroglou and Payatakes, 1990; Liu et al., 1993). Pore network simulators are usually cumbersome, and iterative runs are needed until the produced theoretical curves match satisfactorily the experimental ones for certain parameter values of network models (Ioannidis and Chatzis, 1993a; Jonas and Schopper, 1994; Ridgway and Matthews, 1997; Tsakiroglou and Payatakes, 2000).

An alternative approach to the same problem is the development of closed parametric integral equations describing analytically the N_2 sorption isotherms (Liu et al., 1993) and capillary pressure curves (Larson and Morrow, 1981; Mishra and Sharma, 1988). Such equations can be derived with the aid of percolation theory (Stauffer and Aharony, 1992) by taking into account the specific features of pore geometry (e.g., pore shape factors and pore-size distributions) and incorporating the pore network topology and spatial pore-size correlations into the accessibility functions (Chatzis and Dullien, 1985; Yanuka, 1989a,b; Seaton, 1991; Renault, 1991; Ioannidis et al., 1993b).

Porous materials originating from the consolidation of particles (such as, sintered materials, pelletized materials, agglomerates), exhibit cusps rather than microroughness along pore walls. Such porous media are better modeled by using convex (such as, triangles and higher-order polygons) or concave (such as, packings of spheres; Mason, 1971) surfaces. It is well known that, the capillary properties of irregular pores depend strongly on details of the pore-wall geometry (Cebeci, 1980; Ioannides and Chatzis, 1993; Tsakiroglou and Payatakes, 1993). The rigorous determination of the exact shape of the interface at equilibrium in a polygonal pore requires that the Young-Laplace equation be integrated with the appropriate boundary conditions (Orr et al., 1975; Wong et al., 1992). Instead of this exact but computationally intensive procedure, an approximate method, which was initially proposed for packings of equal spheres (Mayer and Stowe, 1965, 1966), is usually adopted, where the critical radius of curvature for drainage is determined by a force balance along the pore axis. This method has been used successfully for the determination of the drainage and imbibition capillary pressures in square tubes (Legait, 1983), equilateral triangular capillaries (Ransohoff et al., 1987), irregular triangular tubes (Mason and Morrow, 1991), nonaxisymmetric converging–diverging pore geometries formed between solid spheres (Mason and Morrow, 1994), and lenticular pores (Tsakiroglou et al., 1997; Tsakiroglou and Payatakes, 1998).

Hg porosimetry and N_2 sorption experiments are routine analysis techniques used in the development and production control of heterogeneous catalysts, adsorbents, membranes, and so forth. Information about the pore structure is essential for reaction processes, which are to some extent transport limited, due to pore diffusion. This is generally true for a wide range of heterogeneously catalyzed processes, and some examples are: the oil hydrodesulfurization in refineries, where alumina is widely used as support of material of cobalt- and nickel-molybdenum catalysts; the steam reforming of hydrocarbons to synthesis gas, where nickel supported on various porous ceramic materials is used as catalyst. In addition, information concerning the pore structure is also essential for optimizing the production of heterogeneous catalysts, because many unit-operations, such as drying or impregnation, are sensitive to the pore-structure properties.

For the catalyst manufacturers and chemical industry, the pore structure of catalyst carriers is of key importance for the product and process optimization. Therefore, it is desirable to extract as much information as possible from Hg porosimetry curves and N_2 sorption isotherms of each analyzed material. In particular, except for a simple pore-size distribution, information concerning the uniformity of the pore system, pore-size correlations, and pore-network connectivity would be helpful in the quality control of any industrially produced porous material. However, in spite of the high degree of sophistication that has been embedded into several approaches of pore-structure analysis (Mason, 1988; Liu et al., 1992; Rigby, 2000), no systematic procedure has yet been developed to combine Hg porosimetry with N_2 sorption data in such a consistent way that unique geometrical and topological properties of the pore structure are derived.

In the present work, a methodology is developed for the determination of the pore-structure parameters of porous materials expressed in terms of the statistical properties of a pore network, using N_2 sorption and Hg porosimetry data. The parameters are estimated successively by fitting analytical models of the N_2 adsorption/desorption and Hg intrusion processes to one or more sets of experimental data, each time. First, initial guesses of the pore-radius distribution and pore-shape factors are estimated from the N_2 adsorption curve, initial guesses of the throat-radius distribution and accessibility functions are estimated from the Hg intrusion and N_2 desorption curves, and all parameters are updated by fitting the model predictions to all experimental data available. The methodology is evaluated and calibrated with respect to the data of well-known theoretical pore networks, and is subsequently applied to the characterization of the pore structure of four samples of industrially produced porous alumina, which is used as catalyst carrier.

Model of the Pore Structure

The pore structure is represented by a stochastic network of pores (sites) and throats (bonds), the sizes of which are sampled from a site, $f_s(r)$, and a bond radius, $f_b(r)$, distribution function, respectively, either randomly (uncorrelated networks) or nonrandomly (correlated networks). The radius, r, is the characteristic pore dimension that controls all critical pore-scale phenomena of phase transformation during N_2 adsorption/desorption and fluid redistribution during mercury intrusion.

The throats are considered as narrow constrictions without volume. The pores are assigned the entire pore volume according to the relation

$$V_s(r) \propto r^{\beta_s}, \tag{1}$$

where β_s is a volume shape factor ($\beta_s \geq 0$). The volume-shape factor provides information about the dependence of a critical pore dimension on the pore volume. For instance, if the pores are long capillaries, and their radius is defined as the critical dimension, then $\beta_s = 2.0$. For pores formed between spherical particles touching each other, it is $\beta_s \cong 3.0$.

The topological and correlational properties of the pore network are embedded into the bond and site cumulative accessibility functions (Chatzis and Dullien, 1985; Yanuka, 1989a), which, in turn, also depend on the type of percolation process considered (such as bond percolation, site percolation, mixed bond site percolation). Monte Carlo computer simulations in large lattices are required for correlating the accessibility functions with the topology of pore networks (Li et al., 1986; Stauffer and Aharony, 1992; Tsakiroglou and Fleury, 1999).

At a first approach, all pores and throats are represented by long capillaries of identical shape ($\beta_s = 2.0$), and afterwards, the relationships are generalized to any β_s value. The cross section of each pore is modeled by a high-order regular polygon (Figure 1) with parameters: (1) the number of its sides (angles), n_s; (2) the area, A; and (3) the perimeter, P. The pore-shape factor, G (Mason and Morrow, 1991), is given by

$$G = \frac{A}{P^2} \tag{2}$$

and the pore radius, r, is defined as the radius of the inscribed circle in the regular polygon (Figure 1), given by

$$r = 2GP. \tag{3}$$

From the geometry of the polygon (Figure 1), one has

$$G = \frac{1}{4n_s \tan\left(\dfrac{\pi}{n_s}\right)} \tag{4}$$

which results in

$$\frac{dG}{dn_s} = \frac{4[(\pi/n_s) - \sin(\pi/n_s)\cos(\pi/n_s)]}{[4n_s\tan(\pi/n_s)]^2\cos^2(\pi/n_s)} \geq 0, \qquad n_s \geq 3 \tag{5}$$

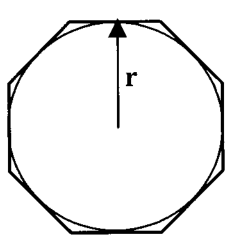

Figure 1. Pore and throat cross-section model.

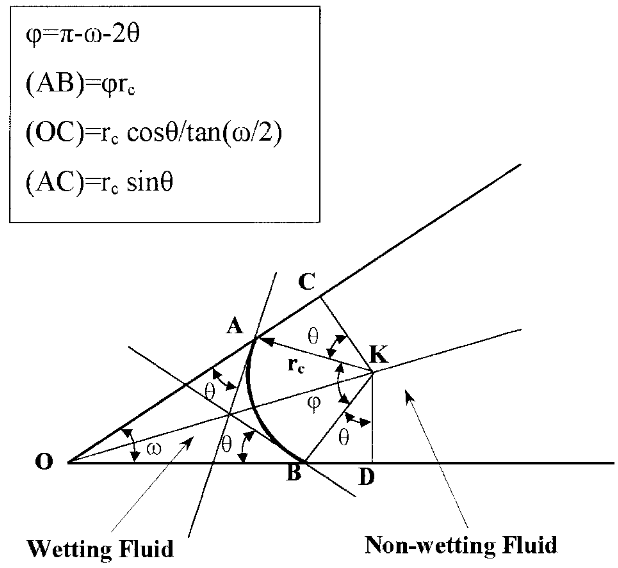

Figure 2. Cross section of a meniscus within the cusp of a polygonal pore.

Therefore, the shape factor, G, is a monotonically increasing function of n_s and takes on a maximum value at the limit $n_s \rightarrow \infty$. From Eq. 4 we get

$$\lim_{n_s \to \infty} G = \frac{1}{4\pi} \tag{6}$$

and hence

$$0 < G \leq 1/4\pi \tag{7}$$

In addition, the angle of pore cusps, ω (Figure 2), is given by

$$\omega = \frac{(n_s - 2)\pi}{2n_s} \tag{8}$$

The number of the sides of a polygonal pore should be regarded as a measure of the pore-wall angularity (or fraction of porosity belonging to pore edges) rather than as an accurate geometrical representation of the pore shape.

The radii of pores formed between touching or interpenetrating solid particles follow a distribution function $f_s(r; \mu_s, \sigma_s)$. Respectively, the radii of throats ("windows") connecting adjacent pores follow a different distribution function $f_b(r; \mu_b, \sigma_b)$.

Drainage and Imbibition in Polygonal Pores

As the capillary pressure increases, the nonwetting fluid (NWF) penetrates into a polygonal capillary tube, preoccupied by a wetting fluid (WF), when the surface energy of the interfacial configuration is minimized (namely, the capillary pressure exerted on the meniscus takes on its minimum value). This condition allows us to calculate approximately the corresponding critical radius of curvature, $r_c = r_d$ (Figure 2) from the relation (Mason and Morrow, 1991; Ransohoff et al., 1987; Tsakiroglou et al., 1997)

$$r_d = \frac{A_{\text{eff}}}{P_{\text{eff}}} \tag{9}$$

where the cross-section area of NWF, A_{eff}, and the effective length of the WF/NWF interfacial zone, P_{eff}, are given by (Figure 2)

$$A_{\text{eff}} = A - \sum_{i=1}^{i=n_s} A_{wi} \tag{10}$$

$$P_{\text{eff}} = \sum_{i=1}^{i=n_s} L_{WNi} + \left(P - \sum_{i=1}^{i=n_s} L_{WSi}\right)\cos\theta \tag{11}$$

respectively. In the preceding relations, A_{wi} is the WF-occupied cross-section area of the pore cusps (namely, the area of the curved triangle OAB; Figure 2), L_{WNi} is the length of the interface formed between the WF and NWF (namely, the length of the arc AB; Figure 2), and L_{WSi} is the wetted perimeter of the solid wall (namely, the total length of lines OA and OB; Figure 2). From geometrical considerations (Figure 2) and after some manipulation, one finally obtains

$$A_{\text{eff}} = A - Fr_d^2 \tag{12}$$

$$P_{\text{eff}} = P - 2Fr_d \tag{13}$$

where the coefficient F depends on the contact angle θ and pore geometry according to

$$F = n_s\left[\frac{\cos\theta\sin\left(\dfrac{\pi}{n_s} - \theta\right)}{\cos\left(\dfrac{\pi}{n_s}\right)} - \left(\frac{\pi}{n_s} - \theta\right)\right] \tag{14}$$

The meniscus remaining within the pore cusps must be convex, namely $\theta \leq \pi/n_s$ and the fraction of the pore cross-section area occupied by the wetting fluid must be positive, namely $F \geq 0$. Otherwise, neither the curvature radius, r_c, nor the NWF saturation are influenced by the presence of pore cusps. By introducing Eqs. 12 and 13 in Eq. 9, we get

$$r_d = r\,\frac{\cos\theta - \sqrt{\cos^2\theta - 4FG}}{4FG} \quad \text{if} \quad F \geq 0 \quad \text{and} \quad \theta \leq \pi/n_s \tag{15a}$$

$$r_d = \frac{r}{2\cos\theta} \quad \text{if} \quad F < 0 \quad \text{or} \quad \theta > \pi/n_s. \tag{15b}$$

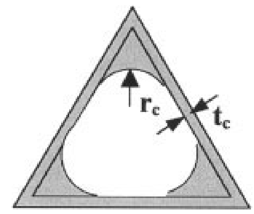

Figure 3. Multilayer adsorption and capillary condensation on a triangular pore.

In triangular and lenticular pores, the critical curvature radius of imbibition, $r_c = r_i$, is determined by the coalescence of the various menisci retracting from the pore cusps and the induced snap-off of the NWF thread because of interfacial instability (Mason and Morrow, 1991; Tsakiroglou et al., 1997). In this manner, thermodynamic pore-level hysteresis is introduced into the models (Everett and Haynes, 1972). Although the retraction of the NWF from an irregular polygonal pore is a more complex process, we assume that menisci unite and the pore empties through snap-off (Tsakiroglou and Payatakes, 1990, 1998) when the total wetted perimeter of the solid wall exceeds the perimeter of the pore, namely

$$\sum_{i=1}^{n_s} L_{WSi} = P \tag{16}$$

By using geometrical arguments analogous to those used in drainage and after some manipulation, one obtains

$$r_i = \frac{r}{4G[F + (\pi - n_s\theta)]} \quad \text{if} \quad F \geq 0 \quad \text{and} \quad \theta \leq \pi/n_s \tag{17a}$$

$$r_i = \frac{r}{2\cos\theta} \quad \text{if} \quad F < 0 \quad \text{or} \quad \theta > \pi/n_s \tag{17b}$$

Analytical Models

N_2 Adsorption/desorption

The multilayer adsorption/desorption of gas molecules on the internal surface of porous solids is of secondary significance for mesoporous (2 nm $< r <$ 50 nm) and macroporous ($r >$ 50 nm) materials, but becomes the crucial mechanism of pore filling in microporous materials ($r <$ 2 nm). Since the classic thermodynamic methods may fail to describe realistically the multilayer adsorption and capillary condensation in micropores, the distribution of gas molecules in a system at equilibrium is commonly determined by using Monte Carlo and molecular-dynamics methods (Steele and Bojan, 1997; Miyahara et al., 1997). Also, the density functional theory offers a practical alternative (Jessop et al., 1991; Webb and Orr, 1997) to the aforementioned methods.

In general, the filling of pores with liquid nitrogen is carried out through two parallel mechanisms (Figure 3): (1) multilayer surface adsorption of gas molecules on the flat pore walls, and (2) capillary condensation of liquid on the rough regions of the adsorbed layer. The thickness of the adsorbed layer, t_c, (Figure 3) is determined by the generalized FHH equation (Gregg and Sing, 1982)

$$t_c = \sigma\left[\frac{b}{\ln(1/x)}\right]^{1/s}, \tag{18}$$

where x is the relative vapor pressure, σ is the diameter of nitrogen molecule (σ = 3.54 A); b is a parameter depending on the properties of the adsorbent and adsorptive, but in practice is of empirical origin; and s is an index with values ranging from 2 to 3 (Gregg and Sing, 1982). The presence of micropores appears to distort the universal t-curve and correlations of index, s, with fractal properties of the pore space have to be taken into account.

The curvature radius of the liquid/vapor menisci of the condensate, r_c, (Figure 3) is given by Kelvin equation (Gregg and Sing, 1982)

$$r_c = \frac{V_L^0\gamma_{\mathrm{LG}}}{RT\ln(1/x)} \tag{19}$$

For the sake of clarity and physical inspection of the produced equations, fluid saturation is first calculated for $\beta_s = 2.0$ and then the equation is generalized to any β_s value. The cross-section areas and perimeters of the two polygons (Figure 3) must satisfy the mass balance

$$A_t = A - t_c\left(\frac{P_t + P}{2}\right) \tag{20}$$

and the condition of similarity (Mason and Morrow, 1991)

$$G = \frac{A}{P^2} = \frac{A_t}{P_t^2} \tag{21}$$

From Eqs. 20 and 21

$$P_t = P - \frac{1}{G}\frac{t_c}{2} \tag{22}$$

is obtained. The saturation of a partially liquid (WF)-occupied pore consists of the adsorbed and condensed phases and is given by

$$S_{f2} = \frac{Fr_c^2 + t_c\left(\frac{P + P_t}{2}\right)}{A} \tag{23}$$

which in combination with Eq. 22 yields

$$S_{f2}(r,\, r_c) = \frac{4F_{\mathrm{LG}}Gr_c^2 + 2rt_c - t_c^2}{r^2} \tag{24}$$

where

$$F_{\mathrm{LG}} = F(\theta = \theta_{\mathrm{LG}}) \tag{25}$$

With the aid of Eqs. 18 and 19, Eq. 24 is transformed to

$$S_{f2}(r,\, r_c) = \frac{4F_{\mathrm{LG}}Gr_c^2 + 2r\sigma(b/c)^{1/s}r_c^{1/s} - [\sigma(b/c)^{1/s}r_c^{1/s}]^2}{r^2} \tag{26}$$

where

$$c = \frac{V_L^0\gamma_{\mathrm{LG}}}{RT} \tag{27}$$

Assuming that any changes of fluid volume in a pore are described by a relation analogous to Eq. 1, Eq. 26 can be read as

$$S_{f2}(r,\, r_c) = \frac{4F_{\mathrm{LG}}Gr_c^{\beta_s} + 2r\sigma(b/c)^{1/s}r_c^{1/s} - [\sigma(b/c)^{1/s}r_c^{1/s}]^{\beta_s}}{r^{\beta_s}} \tag{28}$$

Capillary condensation in a pore is analogous to WF (liquid nitrogen) imbibition. Therefore, the critical curvature radius of condensation, $r_c = r_{\mathrm{con}}$, is obtained from Eq. 17 by taking into account the thickness of the adsorbed layer, t_c, namely

$$r_{\mathrm{con}} = \frac{r - t_c}{4G[F_{\mathrm{LG}} + (\pi - n_s\theta)]} \quad \text{if} \quad F_{\mathrm{LG}} \geq 0 \quad \text{and} \quad \theta \leq \pi/n_s \tag{29a}$$

$$r_{\mathrm{con}} = \frac{r - t_c}{2\cos\theta_{\mathrm{LG}}} \quad \text{if} \quad F_{\mathrm{LG}} < 0 \quad \text{and} \quad \theta > \pi/n_s \tag{29b}$$

Equation 29, in conjunction with Eqs. 18 and 19, yields the critical radius $r = r_s$, given by

$$r_s = 4G[F_{\mathrm{LG}} + (\pi - n_s\theta)]r_{\mathrm{con}} + \sigma(b/c)^{1/s}r_{\mathrm{con}}^{1/s} \quad \text{if} \quad F_{\mathrm{LG}} \geq 0 \quad \text{and} \quad \theta \leq \pi/n_s \tag{30a}$$

$$r_s = 2\cos\theta_{\mathrm{LG}}r_{\mathrm{con}} + \sigma(b/c)^{1/2}r_{\mathrm{con}}^{1/s} \quad \text{if} \quad F_{\mathrm{LG}} < 0 \quad \text{and} \quad \theta > \pi/n_s \tag{30b}$$

During N_2 adsorption, all pores are accessible to the vapor phase at any stage of the process. When an isolated cluster of vapor-occupied pores is surrounded by liquid condensate then, as the vapor relative pressure increases, pore filling may occur by a combination of successive events, including capillary condensation and viscous flow (Everett, 1975). The liquid nitrogen saturation of a pore network as a function of the relative vapor pressure can be expressed by the relation

$$S_{\mathrm{LN2}}(x) = \frac{\int_0^{r_s} f_s(r)V_s(r)\,dr + \int_{r_s}^{\infty} f_s(r)V_s(r)S_{f2}(r)\,dr}{\int_0^{\infty} f_s(r)V_s(r)\,dr} \tag{31}$$

The capillary evaporation from a pore is analogous to the WF drainage, and hence the critical curvature radius of evaporation, r_{evp}, is obtained from Eq. 15 by accounting for the thickness of adsorbed layer, t_c, namely

$$r_{evp} = (r - t_c)\frac{\cos\theta_{LG} - \sqrt{\cos^2\theta_{LG} - 4F_{LG}G}}{4F_{LG}G} \quad \text{if} \quad F_{LG} \geq 0 \quad \text{and} \quad \theta \leq \pi/n_s \tag{32a}$$

$$r_{evp} = \frac{(r - t_c)}{2\cos\theta_{LG}} \quad \text{if} \quad F_{LG} < 0 \quad \text{and} \quad \theta > \pi/n_s \tag{32b}$$

which in conjunction with Eqs. 18 and 19 results in

$$r_b = \frac{4F_{LG}Gr_{evp}}{(\cos\theta_{LG} - \sqrt{\cos^2\theta_{LG} - 4F_{LG}G})} + \sigma(b/c)^{1/s}r_{evp}^{1/s} \quad \text{if} \quad F_{LG} \geq 0 \quad \text{and} \quad \theta \leq \pi/n_s \tag{33a}$$

$$r_b = 2\cos\theta_{LG}r_{evp} + \sigma(b/c)^{1/s}r_{evp}^{1/s} \quad \text{if} \quad F_{LG} < 0 \quad \text{and} \quad \theta > \pi/n_s \tag{33b}$$

where r_b is the critical radius for N_2 evaporating from throats with $r \geq r_b$.

N_2 desorbs from a pore if its radius is less than the critical size (r_b or r_s) and has access either to the bulk vapor phase (primary desorption) or to isolated vapor pockets (secondary desorption). Hence, pore network accessibility properties affect capillary evaporation from pores and contribute significantly to hysteresis phenomena between adsorption and desorption curves (Mason, 1982). At any stage of the desorption process, the fraction of bonds (throats), q_b, and sites (pores), q_s, that are "allowable" to the vapor phase are given by

$$q_b = \int_{r_b}^{\infty} f_b(r)\, dr \tag{34}$$

and

$$q_s = \int_{r_s}^{\infty} f_s(r)\, dr \tag{35}$$

respectively. The fractions of bonds and sites occupied by the vapor phase at the end of the adsorption process are equal to the corresponding fractions of allowable throats, q_{bi} and pores q_{si}, namely

$$Y_{bi}(q_b = q_{bi}) = q_{bi} \quad \text{and} \quad Y_{si}(q_s = q_{si}) = q_{si} \tag{36}$$

where

$$q_{bi} = \int_{r_{bi}}^{\infty} f_b(r)\, dr \tag{37}$$

and

$$q_{si} = \int_{r_{si}}^{\infty} f_s(r)\, dr \tag{38}$$

The pore sizes r_{bi} and r_{si} are given by Eq. 30 at the maximum relative pressure of adsorption x_f. The fractions of accessible bonds (throats), Y_{bi}, and sites (chambers), Y_{si}, to the vapor phase as functions of the fractions of allowable ones q_b and q_s are the accessibility functions of the pore network and are usually calculated from Monte Carlo simulations (Mason, 1982). According to percolation theory (Seaton, 1991; Stauffer and Aharony, 1992; Sahimi, 1993), these functions are affected by the network topology, spatial pore-size correlations, and network size.

Given that the pore volume is assigned exclusively to pores (sites), only the accessibility function $Y_{si}(q_b)$ is included in the calculation of the liquid N_2 saturation. At each step of desorption, the liquid-occupied pore volume is equal to the sum of (1) the volume of condensate remaining in pores with sizes $r \leq r_s$; (2) the volume of N_2 adsorbed on the pore walls of partially liquid-occupied pores, with sizes $r > r_s$; and (3) the volume of condensate in pores that are not accessible to the vapor phase and have sizes $r > r_s$. Consequently, the liquid nitrogen saturation in a pore network as a function of the relative vapor pressure is given by

$$S_{LN2}(x) = \frac{\int_0^{r_s} f_s(r)V_s(r)\, dr + \dfrac{q_s - Y_{si}(q_b)}{q_s - q_{si}}\int_{r_s}^{r_{si}} f_s(r)V_s(r)\, dr + \dfrac{Y_{si}(q_b)}{q_s}\int_{r_s}^{\infty} f_s(r)V_s(r)S_{f2}(r)\, dr}{\int_0^{\infty} f_s(r)V_s(r)\, dr} \tag{39}$$

where the critical pore radius, r_s, is given by

$$r_s = r_{si} \quad \text{if} \quad r_b > r_{si} \tag{40a}$$

$$r_s = r_b \quad \text{if} \quad r_b \leq r_{si} \tag{40b}$$

Mercury intrusion

The process is analogous to capillary evaporation for $q_{si} = 0$ (primary desorption) and is controlled by throat sizes. The mercury saturation in a pore network is given by

$$S_{Hg}(P_c) = 1 - \frac{\int_0^{r_s} f_s(r)V_s(r)\, dr + \dfrac{q_s - Y_{s0}(q_b)}{q_s}\int_{r_s}^{\infty} f_s(r)V_s(r)\, dr + \dfrac{Y_{s0}(q_b)}{q_s}\int_{r_s}^{\infty} f_s(r)V_s(r)S_{f1}(r)\, dr}{\int_0^{\infty} f_s(r)V_s(r)\, dr} \tag{41}$$

where

$$r_c = \frac{\gamma_{Hg}}{P_c} \tag{42}$$

$$F_{Hg} = F(\theta = \theta_{Hg}) \tag{43}$$

$$r_b = \frac{4F_{Hg}Gr_c}{(\cos\theta_{Hg} - \sqrt{\cos^2\theta_{Hg} - 4F_{Hg}G})} \quad \text{if} \quad F_{Hg} > 0 \quad \text{or} \quad \theta_{Hg} < \pi/n_s \tag{44a}$$

$$r_b = 2r_c\cos\theta_{Hg} \quad \text{if} \quad F_{Hg} < 0 \quad \text{or} \quad \theta_{Hg} \geq \pi/n_s \tag{44b}$$

$$r_s = r_b \tag{45}$$

$$S_{f1}(r, r_c) = 4F_{Hg}G\left(\frac{r_c}{r}\right)^{\beta_s} \quad \text{if} \quad F_{Hg} > 0 \quad \text{or} \quad \theta_{Hg} < \pi/n_s \tag{46a}$$

$$S_{f1}(r, r_c) = 0 \quad \text{if} \quad F_{Hg} < 0 \quad \text{or} \quad \theta_{Hg} \geq \pi/n_s \tag{46b}$$

Accessibility functions

From pore-network simulations, it is well known that the pore-space topology and spatial pore-size correlations are introduced implicitly into the site accessibility functions of primary drainage Y_{s0} and secondary desorption Y_{si}. Pore network simulations have revealed that accessibility functions can be described satisfactorily by sigmoid curves of the form

$$Y_{si}(q_b) = \frac{q_{si}^0 + (1 + a_i - q_{si}^0)e^{-b_i(1-q_b)/q_b}}{1 + a_ie^{-b_i(1-q_b)/q_b}} \tag{47}$$

where q_{si}^0 is the initial fraction of sites occupied by the NW phase ($q_{si}^0 = 0$ for primary drainage and desorption, and $q_{si}^0 = q_{si}$ for secondary desorption initiating before the completion of adsorption). Two quantitative measures of the relative position of each accessibility function are (1) the "percolation threshold," $q_b = q_{bci}$, which corresponds to the inflection point of the curve $(d^2Y_{si}/dq_b^2)_{q_b=q_{bci}} = 0$; and (2) the slope of the accessibility function at the percolation threshold, λ_{bci}. These two parameters are obtained from the numerical solution of the following equations

$$b_i - 2z_c - (2z_c + b_i)a_ie^{-b_i/z_c} = 0 \tag{48}$$

$$\lambda_{bci} = \frac{b_i(a_i + 1)(1 - q_{si})e^{-b_i/z_c}}{z_c^2(1 + a_ie^{-b_i/z_c})^2} \tag{49}$$

$$z_c = \frac{q_{bci}}{1 - q_{bci}} \tag{50}$$

Simulation of mercury intrusion and primary/secondary desorption in uncorrelated and *c–t* correlated cubic networks allowed us to determine realistic accessibility functions, which, in turn, were fitted to the analytic functions of Eq. 47. In *c–t* correlated networks the percolation threshold is lower and the accessibility function is wider than the corresponding ones of uncorrelated networks (Tables 1 and 2).

Table 1. Parameter Values of the Site Accessibility Functions of Secondary Desorption Y_{si}, Obtained by Fitting Eq. 47 to Results of Ten Realizations in 30 × 30 × 30 Uncorrelated Pore Networks

q_{si}	a_i	b_i	q_{bci}	λ_{bci}
0.0	707.709	2.5890	0.27	8.479
0.0005	673.4	2.5635	0.269	8.43
0.005	240.216	2.0604	0.256	7.407
0.05	28.195	1.0499	0.202	5.68
0.1	12.912	0.734	0.171	5.317
0.2	6.477	0.5078	0.140	5.174
0.3	4.912	0.4363	0.129	5.146
0.4	4.743	0.4279	0.127	5.144
0.5	5.325	0.4581	0.133	5.136
0.6	6.877	0.5382	0.146	5.089
0.7	9.985	0.6870	0.169	5.015

Table 2. Parameter Values of the Site Accessibility Functions of Secondary Desorption Y_{si}, Obtained by Fitting Eq. 47 to Results of Ten Realizations in 30 × 30 × 30 *c–t* Correlated Pore Networks

q_{si}	a_i	b_i	q_{bci}	λ_{bci}
0.0	14.866	0.928	0.1942	4.845
0.0005	14.110	0.906	0.1921	4.819
0.005	10.958	0.802	0.1808	4.711
0.05	1.485	0.305	0.107	4.202
0.1	0.294	0.192	0.082	4.054
0.2	0.352	0.217	0.0909	3.776
0.3	0.7148	0.290	0.1116	3.497
0.4	1.0335	0.3708	0.1333	3.234
0.5	1.250	0.4537	0.155	2.985
0.6	1.576	0.575	0.184	2.771
0.7	1.872	0.719	0.214	2.589

Sensitivity analysis

The aforementioned models were used to investigate the effect of each individual parameter on Hg intrusion and N_2 isotherms. The values of the constants included in the foregoing equations are given in Table 3. The individual effect of each parameter of the pore-structure model on N_2 adsorption/desorption and Hg intrusion curves are shown in Figures 4–8. In all calculations the accessibility functions of an uncorrelated regular cubic network (Table 1) were used except if otherwise stated. Most of the effects of pore space parameters on N_2 sorption and Hg intrusion curves have already been identified in earlier studies with the use of pore-network simulations (Liu

Table 3. Values of Constants Embedded in Models

Constant	Value
c	0.47 nm
θ_{LG}	0°
σ	0.354 nm
b	0.5 nm
s	2.0
γ_{Hg}	0.48 Nt/m

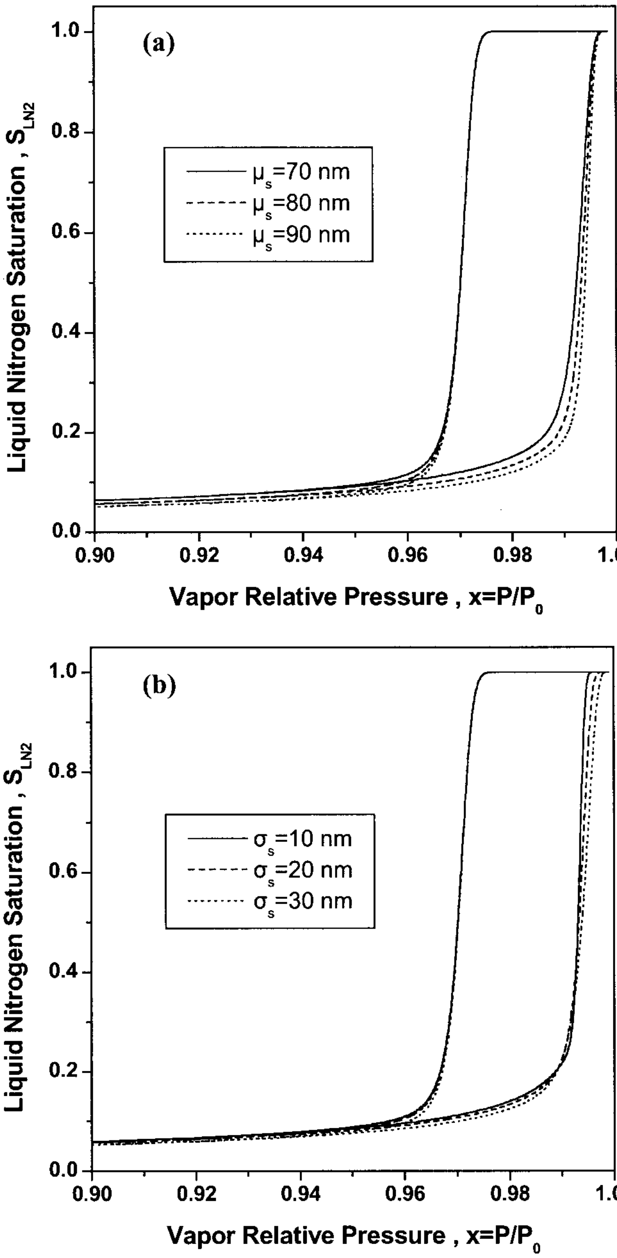

Figure 4. Effect of the (a) mean value, and (b) standard deviation of the pore radius distribution on N_2 isotherms.

et al., 1992, 1993; Tsakiroglou and Payatakes, 2000), and for this reason any detailed explanation is omitted here. Changes on the $f_s(r;\ \mu_s,\ \sigma_s)$ are reflected in N_2 adsorption curve (Figure 4a and 4b), while changes on the $f_b(r;\ \mu_b,\ \sigma_b)$ are reflected in N_2 desorption (Figure 5a and 5c) and Hg intrusion (Figure 5b and 5d) curves. The variation of parameter n_s affects primarily the width of N_2 adsorption curve (Figure 6a), and secondarily the position of N_2 desorption and Hg intrusion curves (Figure 6a and 6b). It is worth noting the strong sensitivity of primary (Figure 7b and 7c) and secondary (Figure 7d) curves to accessibility functions (Figure 7a), as well as the interactive effects of n_s and θ_{Hg} on Hg intrusion curve (Figure 8a and 8b). The results of the sensitivity analysis (Figures 4–8) enabled us to construct a covariance matrix (Table 4) and use it as a guideline for the development of various numerical schemes of parameter estimation.

Parameter Estimation

There is a variety of deterministic (such as least squares) or stochastic (such as Bayesian) methods of parameter estimation for nonlinear problems (Bard, 1974). ATHENA visual workbench software (Stewart et al., 1996) is a fully integrated environment for process modeling and nonlinear parameter estimation, is fully automated, and requires a Fortran compiler to operate. The software includes the solver GREGPLUS for the nonlinear parameter estimation with weighted least-square or/and Bayesian estimators (Bard, 1974; Stewart et al., 1992, 1996, 1998). GREGPLUS computes modal and interval estimates of the parameters in a user-provided Fortran subroutine MODEL, for single- or multiresponse observations.

The objective function (Bard, 1974), a weighted sum of square residuals (least-square method) or sample covariance determinants (Bayesian estimation), is expanded as a quadratic function of the parameters around the initial parameter values of the current iteration. The parametric sensitivities needed for this step can be generated by GREGPLUS with optimized divided-difference steps; alternatively some or all of them can be provided by the user's subroutine MODEL. The resulting minimization problem is solved with successive quadratic programming (QP), starting from the user's guesses for the parameters and using a modified Gauss-Jordan algorithm (Bard, 1974).

Because of the large number of parameters involved in the pore structure model, the straightforward derivation of reliable estimates for them from mercury intrusion and nitrogen sorption data is a laborious task. Instead, the problem can be highly simplified by dividing it into a number of subproblems of lower difficulty. Based on the sensitivity analysis and parameter covariance matrix (Table 4), the set of parameters was divided into two subsets, and each subset was estimated by using only one or two sets of experimental data. It was decided to estimate the parameters μ_s, σ_s, n_s, β_s from the N_2 adsorption curve, and the parameters μ_b, σ_b, q_{bc0}, λ_{bc0}, q_{bci}, λ_{bci} from the N_2 desorption/mercury intrusion curves.

Initial guess of the accessibility function

One of the difficulties encountered in multiparameter estimation problems is the selection of rational initial guesses for parameter values. In this manner, the time of numerical calculations is reduced substantially, whereas the probability of obtaining the "true" (global) optimum solution increases. Initial guesses of the size distributions $f_s(r;\ \mu_s,\ \sigma_s)$ and $f_b(r;\ \mu_b,\ \sigma_b)$ can be obtained easily by differentiating the experimental N_2 adsorption and N_2 desorption (or Hg intrusion) curves, respectively. Moreover, the analytic mathematical models of the corresponding processes can contribute to the selection of an initial guess of the accessibility function, which is consistent with the corresponding guess of the throat-size distribution.

The analytic mathematical models of N_2 adsorption/desorption express the saturation of a network with liquid nitrogen as

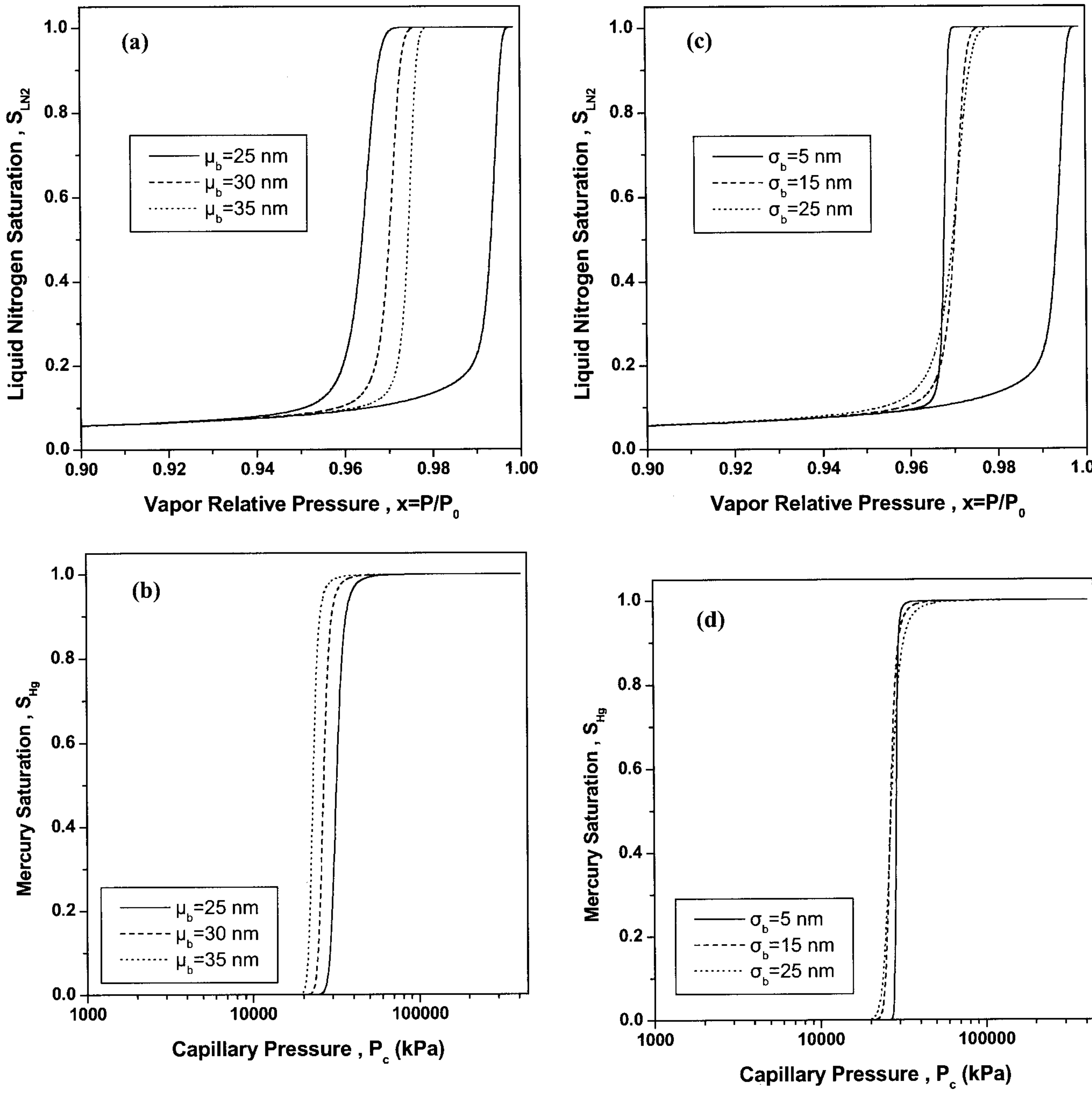

Figure 5. Effect of the (a), (b) mean value, and (c), (d) standard deviation of the throat radius distribution on N_2 isotherms and Hg intrusion curve.

a function of the relative vapor pressure. Assuming that (1) the N_2 saturation values coincide with the corresponding experimental data of the investigated pore structure, and (2) the geometrical parameters introduced in the aforementioned equations (pore-size distributions, pore-shape factors, etc) are well known, either as initial guesses or as outputs from an earlier step of the estimation procedure, we can develop a numerical scheme enabling us to get an initial guess of the accessibility function from an initial guess of the throat-size distribution (see the Appendix).

Methodologies of parameter estimation

Numerical codes of nonlinear parameter estimation were developed in the environment of ATHENA. Depending on the mode of selected statistical pore-size distributions (such as unimodal, bimodal), different versions of these codes were developed. In general, the codes can be classified with respect to the data sets used and parameters estimated:

(1) LEV1: It makes use of the N_2 adsorption response, and is used to estimate the set of parameters (μ_s, σ_s, n_s, β_s).

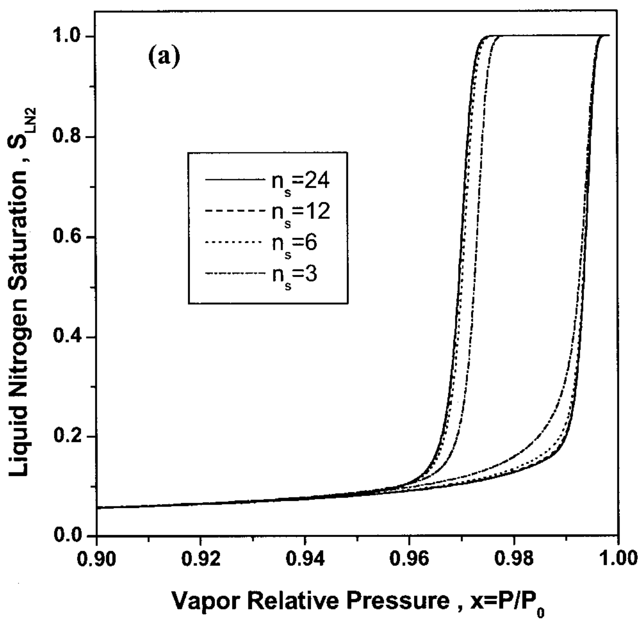

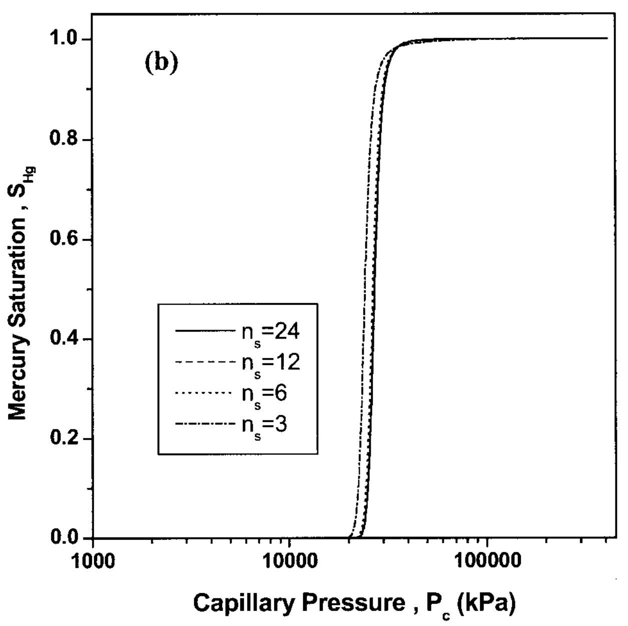

Figure 6. Effect of the number of polygon sides on the (a) N_2 isotherms, and (b) Hg intrusion curve.

(2) LEV23a: It makes use of the N_2 desorption and Hg intrusion responses, and is used to estimate the set of parameters (μ_b, σ_b, q_{bc0}, λ_{bc0}).

(3) LEV23b: It makes use of the N_2 desorption and Hg intrusion responses, and is used to estimate the set of parameters (μ_b, σ_b, q_{bc0}, λ_{bc0}, q_{bci}, λ_{bci}).

(4) LEV2: It makes use of the N_2 desorption response, and is used to estimate the set of parameters (μ_b, σ_b, q_{bci}, λ_{bci}).

(5) LEV3: It makes use of the Hg intrusion response, and is used to estimate the set of parameters (μ_b, σ_b, q_{bc0}, λ_{bc0}).

(6) LEV123: It makes use of the N_2 adsorption/desorption and Hg intrusion responses, and is used to estimate the full set of parameters (μ_s, σ_s, n_s, β_s, μ_b, σ_b, q_{bc0}, λ_{bc0}, q_{bci}, λ_{bci}).

(7) ACCESS: It makes use of the N_2 adsorption/desorption responses to determine an initial guess of the accessibility function $Y_{si}(q_b)$ from the bond-size distribution $f_b(r;\ \mu_b,\ \sigma_b)$ (see the Appendix).

(8) GUESS: It makes use of the foregoing numerical values of the accessibility functions $Y_{si}(q_b)$ or $Y_{s0}(q_b)$ (output of ACCESS) to estimate initial values for the relevant parameters (a_i, b_i, q_{bci}, λ_{bci}) or (a_0, b_0, q_{bc0}, λ_{bc0}).

Two semiempirical multistep estimation procedures, using two or more numerical codes, were devised to minimize the CPU time and ensure the reliability of estimated parameter values. The procedure P1 (Figure 9) was designed to apply to pore structures exhibiting complete (primary) N_2 adsorption/desorption curves, whereas the procedure P2 (Figure 10) was designed to apply to pore structures exhibiting incomplete (secondary) N_2 adsorption/desorption curves.

Three sets of parameter values (Table 5) were selected and fed as input data to the foregoing mathematical models. The resulting N_2 sorption and Hg intrusion curves were regarded as the "experimental" data of "imaginary" pore structures (test samples), and used to evaluate the efficiency of the estimation procedures. The maximum relative vapor pressure was considered equal to 0.9999 for samples Test 1 and Test 2 (primary N_2 adsorption/desorption curves, $q_{si} = 0$) and equal to 0.9995 for sample Test 3 (secondary adsorption/desorption curves, $q_{si} > 0$). The initial guesses of (μ_s, σ_s) and (μ_b, σ_b) were based on the differentiation of the N_2 adsorption and N_2 desorption/Hg intrusion curves, respectively (Table 6). In all cases, the parameter values (μ_s, σ_s, n_s, β_s) estimated by the code LEV1 were in excellent agreement (Table 7) with their corresponding true values (Table 5) almost independently of the initial guess.

From pore network simulations it is well known that the TSD (μ_b, σ_b) obtained with the conventional method of analysis (differentiation of N_2 desorption or Hg intrusion curve) is almost always different from the true one, and the mean value, μ_b, may be smaller or larger than the true value, depending on the interactive effects of pore accessibility (causing movement of the TSD toward smaller sizes) and erroneous attribution of LN2 or Hg saturation changes to throat volume (causing movement of the TSD toward larger sizes). For each sample, the full range of (μ_b, σ_b) is scanned and initial parameter values of the corresponding accessibility functions are produced by using the codes ACCESS and GUESS (Table 8). The upper and lower limits of the ranges of (μ_b, σ_b) are set by the μ_s and the asymptotic values $q_{bc0} \to 0$ and $\lambda_{bc0} \to \infty$ (or $a_0 \to -1$ and $b_0 \to 0$), which correspond to a system of parallel pores of infinite connectivity.

The inherent interrelation of the initial guesses of (μ_b, σ_b) with those of (q_{bc0}, λ_{bc0}) may be associated with the existence of multiple local minima of the objective function (Stewart et al., 1992) and therefore with the existence of more than one optimum values for the set (μ_b, σ_b, q_{bc0}, λ_{bc0}, θ_{Hg}) (Tables 8 and 9). In order to overcome this shortcoming, which is inherent in almost any parameter estimation procedure, the criterion of minimization of the sum of square residuals (SSR) was used to select among them the optimum set (Tables 8 and 9). With reference to the procedure P1 (Figure 9) applied to samples Test 1 and Test 2, the estimated values of the set (μ_s, σ_s, n_s,

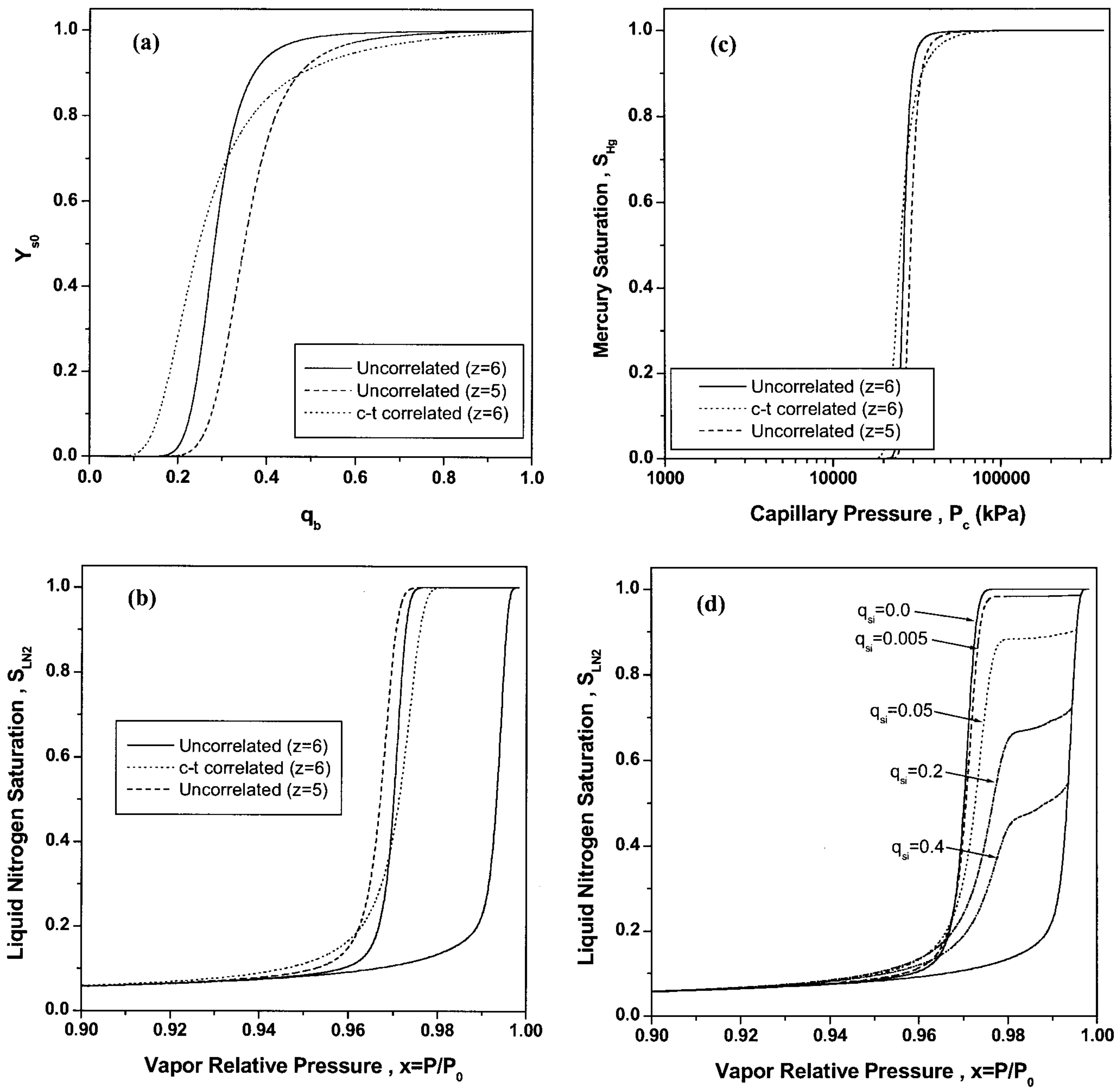

Figure 7. (a) Primary accessibility functions for networks of varying topology and spatial pore-size correlations; (b) effects of the primary accessibility function on N_2 isotherms; (c) effects of the primary accessibility function on Hg intrusion curve; (d) effects of secondary accessibility function on N_2 sorption isotherms.

β_s, μ_b, σ_b, q_{bc0}, λ_{bc0}, θ_{Hg}) were almost identical to their true values (Table 10). Another criterion of the correctness of the estimated parameter values is the minimization of their confidence intervals (Table 10). The narrower the confidence intervals, the greater the probability that the estimated parameter values are close to their true ones. In addition, it is noteworthy that the accurate value of θ_{Hg} was recovered in both cases (Table 10), thanks to the existence of a common accessibility function for N_2 desorption and Hg intrusion.

In applying procedure P2 (Figure 10) to sample Test 3, for each pair of (μ_b, σ_b) values, the N_2 adsorption/desorption data were introduced into the code ACCESS (see the Appendix) and the accessibility function thus produced was fitted with Eq. 47 (code GUESS) to determine initial guesses for (q_{bci}, λ_{bci}) values (Table 11a, left-side columns). Given that, for relatively low q_{si} values, it holds that $q_{bc0} > q_{bci}$ and $\lambda_{bc0} > \lambda_{bci}$ (Tables 1 and 2), the preselection of initial guesses for the parameters (q_{bc0}, λ_{bc0}) (Table 11b) was based on the estimated values of (q_{bci}, λ_{bci}) (Table 11a). Then, two different methods were tested for the introduction of good initial guesses of the set (μ_b, σ_b, q_{bci}, λ_{bci}, q_{bc0}, λ_{bc0}, θ_{Hg}) into the numerical code LEV23b (Figure 10): (1) the parameters (μ_b,

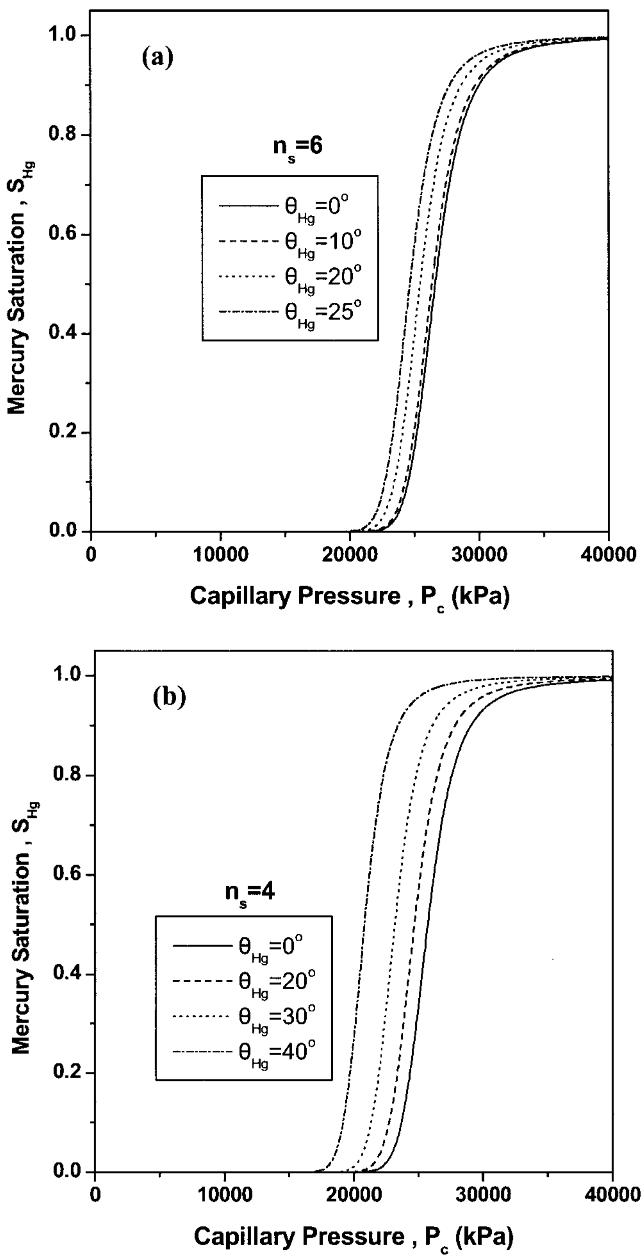

Figure 8. Effect of Hg contact angle on Hg intrusion curve for a pore system composed of pores of (a) hexagonal and (b) rectangular cross section.

σ_b) were kept constant, and initial guesses were determined separately for the sets (q_{bci}, λ_{bci}) and (q_{bc0}, λ_{bc0}, θ_{Hg}) by using the codes LEV2 and LEV3, respectively (Table 11a and 11b); (2) the codes LEV2 and LEV3 were used to estimate the full sets of (μ_b, σ_b, q_{bci}, λ_{bci}) and (μ_b, σ_b, q_{bc0}, λ_{bc0}, θ_{Hg}), respectively (Table 11a and 11b), and the averages of the resulting (μ_b, σ_b) values were introduced into LEV23b as initial guesses. The selection of the optimum set of parameter values was based on the criterion of minimization of the SSR, and the second method was found to be more efficient than the first one (Table 12). This may be associated with the perturbation caused on the local optimum of the parameter vector, by selecting the averages of (μ_b, σ_b) rather than their accurate values resulting from the codes LEV2 or LEV3. The efficiency of procedure P2 is satisfactory (Table 13), considering the large number of parameters and the loss of information embedded

Table 4. Covariance Matrix

Parameter	N_2 Adsorption	N_2 Desorption	Hg Intrusion
μ_s ↑	→	×	×
σ_s ↑	←→	×	×
μ_b ↑	×	→	←
σ_b ↑	×	←→	←→
q_{bci} ↑	×	←	×
λ_{bci} ↑	×	→←	×
q_{bc0} ↑	×	←	→
λ_{bc0} ↑	×	→←	→←
n_s ↑	→← ⟶	→← ⟶	→← ⟶
θ_{Hg} ↑	×	×	→← ⟵

Note: → = Shift to higher values of the independent variable; ← = shift to lower values of the independent variable; →← = narrowing; ←→ = broadening; ↑ = increase; ↓ = decrease; × = no effect.

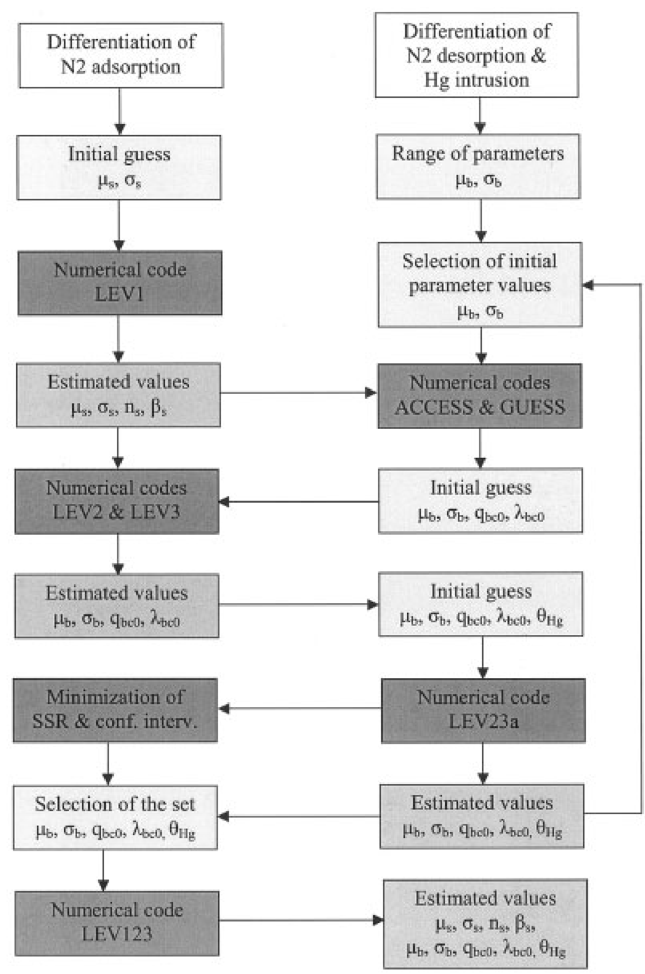

Figure 9. Flowsheet of the P1 multistep estimation procedure used for materials with primary N_2 sorption curves.

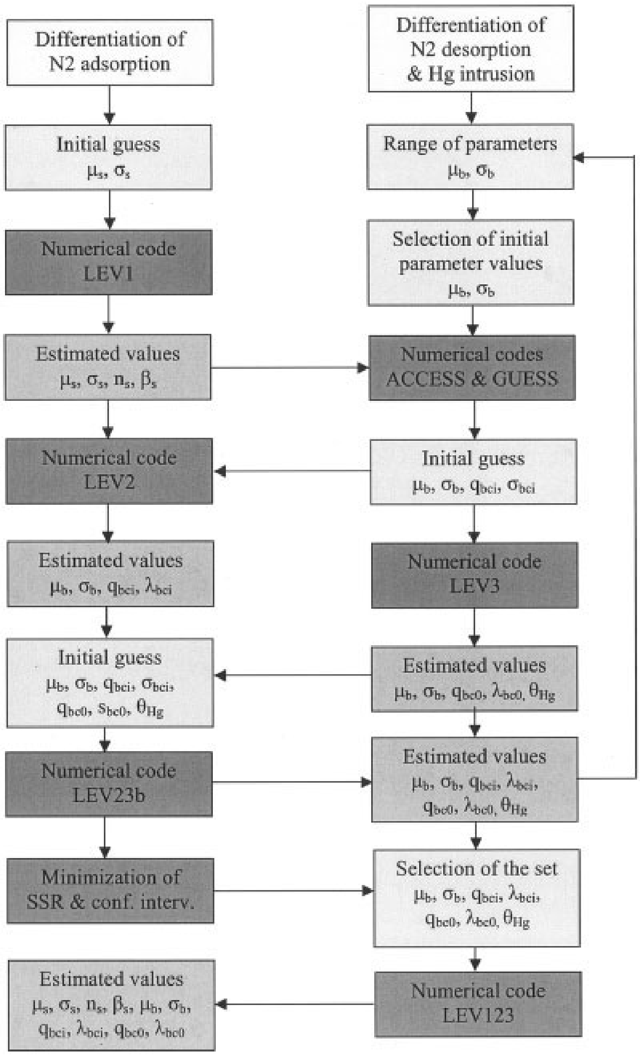

Figure 10. Flowsheet of the P2 multistep estimation procedure used for materials with secondary N_2 sorption curves.

into the last (and not "seen") parts of N_2 adsorption/desorption curves. The estimates were not improved any further by the use of a global optimization final step (code LEV123), that uses the outputs of earlier steps as initial guesses (Figures 9 and 10).

Application to Actual Porous Materials

The N_2 sorption and Hg intrusion curves of four samples of porous alumina, prepared by sintering nonspherical particles under varying conditions (Figure 11) were used to examine the capability of the new methodology to provide unique pore- and throat-size distributions along with additional pore-structure parameters. The analysis described below demonstrates the applicability of the present method to a general class of porous materials originating from the sintering of particles, and having pore shape that is consistent to the geometrical model considered (Figures 1–3). Other geometrical models (e.g., pores with concave shape of the pore-wall solid surface, smooth pores with fractal roughness features superposed on them, etc.) may be adequate to represent other classes of porous materials. Then, the parameter characterizing the pore-wall angularity (n_s) might be replaced by another one (e.g., angle of sharpness, surface fractal dimension, etc.) and equations describing the phenomena at the pore level would change, accordingly. However, the mathematical formulation at the scale of the pore network and the steps of the methodology would remain unaltered.

Table 5. Parameter Values of Theoretical Test Samples

Parameter	Test 1	Test 2	Test 3
μ_s (nm)	80	120	500
σ_s (nm)	20	60	300
n_s	4.0	6.0	4.0
β_s	2.0	2.0	2.0
μ_b (nm)	30	50	50
σ_b (nm)	15	40	40
q_{si}	0.0	0.0	0.074
φ_{si}	0.0	0.0	0.368
q_{bci}–a_i	—	—	0.186–20.86
λ_{bci}–b_i	—	—	5.192–0.898
q_{bc0}–a_0	0.331–210.2	0.203–14.87	0.270–707.7
λ_{bc0}–b_0	6.245–2.884	4.845–0.928	8.479–2.589
θ_{Hg}	0°	40°	40°
x_{max}	0.9999	0.9999	0.9995

Samples with primary N_2 sorption isotherms

The methodology P1 (Figure 9) was processed for the characterization of the pore structure of two porous materials, D and E (Table 14), exhibiting primary (complete) N_2 sorption curves. The total pore volume was assumed equal to the value resulting from N_2 sorption (Table 14), namely $V_p = V_{pN_2}$. The estimated optimum parameter values are shown in Table 15. Lognormal unimodal distribution functions were used for the representation of the statistics of site (pore) and bond (throat) sizes of both samples, whereas the mercury intrusion contact angle was kept constant ($\theta_{Hg} = 40°$). In Figures 12 and 13 experimental data are compared to model predictions for the parameter values of Table 15. The discrepancy observed over the low-pressure region of mercury intrusion curve for sample D (Figure 12b) can be attributed to surface pores that are accessible through large throats. In other words, the entire pore structure is heterogeneous, consisting of a uniform network of fine pores surrounded by a thin layer of large pores. Therefore, a bimodal throat radius distribution and a composite accessibility function should be included in the model to reproduce the low-pressure region of the Hg intrusion curve (Tsakiroglou and Payatakes, 1991b). Likewise, the use of a bimodal throat-size distribution might improve substantially the prediction of the

Table 6. Initial Guesses of Sites, $f_s(r;\ \mu_s,\ \sigma_s)$, and Bond, $f_b(r;\ \mu_b,\ \sigma_b)$ Size Distributions

Parameter (nm)	Test 1	Test 2	Test 3	Origin
μ_s	63.6	131.0	449.2	Differentiation of N_2 adsorption curve
σ_s	30.5	85.0	211.8	Differentiation of N_2 adsorption curve
μ_b	22.5	47.3	126.5	Differentiation of N_2 desorption curve
	33.6	63.5	58.0	Differentiation of Hg intrusion curve
σ_b	5.5	16.0	265.4	Differentiation of N_2 desorption curve
	4.1	15.8	8.0	Differentiation of Hg intrusion curve

Table 7. Estimation of the Parameters (μ_s, σ_s, n_s, β_s) of the Test Samples (Code: LEV1)

Initial Values				Estimated Values			
μ_s (nm)	σ_s (nm)	n_s	β_s	$\mu_s \pm \Delta\mu_s$ (nm)	$\sigma_s \pm \Delta\sigma_s$ (nm)	$n_s \pm \Delta n_s$	$\beta_s \pm \Delta\beta_s$
				Sample: Test 1			
63.6	30.5	12	2.0	$80 \pm 2.4 \cdot 10^{-7}$	$20 \pm 6.5 \cdot 10^{-8}$	$4.0 \pm 6.9 \cdot 10^{-8}$	$2.0 \pm 5.6 \cdot 10^{-10}$
63.6	30.5	100	2.0				
63.6	30.5	12	3.5				
100.0	50.0	100	2.0				
120.0	70.0	12	2.0				
				Sample: Test 2			
131.0	85.0	100	2.0	$120 \pm 5.4 \cdot 10^{-7}$	$60 \pm 8.2 \cdot 10^{-8}$	$6.0 \pm 2.1 \cdot 10^{-7}$	$2.0 \pm 5.4 \cdot 10^{-10}$
131.0	85.0	100	3.0				
180.0	100.0	50	2.5				
				Sample: Test 3			
449.2	211.8	50	3.0	$500 \pm 2.1 \cdot 10^{-5}$	$300 \pm 4.9 \cdot 10^{-6}$	$4.0 \pm 5.6 \cdot 10^{-7}$	$2.0 \pm 5.5 \cdot 10^{-9}$
600.0	500.0	50	2.0				
300.0	150.0	50	2.5				

Table 8. Estimation of the Parameters (μ_b, σ_b, q_{bc0}, λ_{bc0}) of Test 1 (Code: LEV23a)

Initial Values					Estimated Values					
μ_b (nm)	σ_b (nm)	q_{bc0}	λ_{bc0}	θ_{Hg}	μ_b (nm)	σ_b (nm)	q_{bc0}	λ_{bc0}	θ_{Hg}	SSR
15	10	0.053	31.27	0	13.8	10.8	0.053	30.26	0.37	$3.49 \cdot 10^{-5}$
20	10	0.094	16.16	0	17.6	12.3	0.094	17.82	0.29	$2.55 \cdot 10^{-5}$
20	20	0.19	11.9	0	23.8	13.9	0.191	9.51	0.24	$8.80 \cdot 10^{-6}$
25	10	0.174	8.7	0	22.9	13.8	0.174	10.32	0.25	$1.117 \cdot 10^{-5}$
25	20	0.229	12.35	0	25.7	14.3	0.229	8.216	0.197	$4.754 \cdot 10^{-6}$
30	10	0.315	5.303	0	29.4	14.9	0.315	6.464	0.0	$1.247 \cdot 10^{-7}$
30	20	0.324	9.04	0	29.7	14.9	0.324	6.340	0.0	$2.579 \cdot 10^{-8}$
35	10	0.523	4.04	0	36.6	15.9	0.523	5.061	0.0	$1.887 \cdot 10^{-5}$
35	20	0.441	7.275	0	33.9	15.5	0.441	5.308	0.0	$5.892 \cdot 10^{-6}$

Table 9. Estimation of the Parameters (μ_b, σ_b, q_{bc0}, λ_{bc0}) of Test 2 (Code: LEV23a)

Initial Values					Estimated Values					
μ_b (nm)	σ_b (nm)	q_{bc0}	λ_{bc0}	θ_{Hg}	μ_b (nm)	σ_b (nm)	q_{bc0}	λ_{bc0}	θ_{Hg}	SSR
30	30	0.075	12.5	0	27.4	32.5	0.07	13.5	40	$1.1 \cdot 10^{-3}$
30	40	0.090	13.07	0	31.9	34.5	0.090	10.48	40	$8.685 \cdot 10^{-4}$
40	30	0.115	7.34	0	50.0	40.0	0.203	4.838	40	$3.7665 \cdot 10^{-5}$
40	40	0.138	8.012	0	39.3	36.2	0.128	7.272	40	$4.345 \cdot 10^{-4}$
40	50	0.147	8.861	0	50.0	39.9	0.202	4.88	39.9	$7.139 \cdot 10^{-4}$
50	30	0.179	4.518	0	50.0	40.0	0.203	4.84	40	$3.74 \cdot 10^{-5}$
50	50	0.209	6.113	0	50.0	39.9	0.203	4.843	40	$3.945 \cdot 10^{-5}$
50	60	0.209	6.877	0	50.0	40.0	0.203	4.843	40	$3.953 \cdot 10^{-5}$
50	70	0.205	7.595	0	50.0	40.0	0.203	4.839	40	$3.724 \cdot 10^{-5}$
60	30	0.275	2.974	0	50.0	40.1	0.203	4.86	40	$4.148 \cdot 10^{-5}$
60	40	0.289	3.772	0	50.1	40.0	0.203	4.837	40	$3.775 \cdot 10^{-5}$
60	70	0.273	5.815	0	50.0	40.0	0.203	4.844	40	$3.983 \cdot 10^{-5}$
70	70	0.350	4.702	0	50.0	40.0	0.203	4.843	40	$3.996 \cdot 10^{-5}$

Table 10. Comparison of True with Estimated Parameter Values of Test 1 and Test 2

	Sample: Test 1			Sample: Test 2		
Parameter	True Value	Estimated Value	Confidence Interval	True Value	Estimated Value	Confidence Interval
μ_s (nm)	80	80	$2.4 \cdot 10^{-7}$	120	120	$5.4 \cdot 10^{-7}$
σ_s (nm)	20	20	$6.5 \cdot 10^{-8}$	60	60	$8.2 \cdot 10^{-8}$
n_s	4.0	4.0	$6.9 \cdot 10^{-8}$	6.0	6.0	$2.1 \cdot 10^{-7}$
β_s	2.0	2.0	$5.6 \cdot 10^{-10}$	2.0	2.0	$5.4 \cdot 10^{-10}$
μ_b (nm)	30	29.7	$9.05 \cdot 10^{-5}$	50	50.1	$6.9 \cdot 10^{-3}$
σ_b (nm)	15	14.9	$3.2 \cdot 10^{-3}$	40	40.0	$6.9 \cdot 10^{-3}$
q_{bc0}	0.331	0.324	—	0.203	0.203	—
λ_{bc0}	6.245	6.34	$1.07 \cdot 10^{-3}$	4.845	4.838	$8.9 \cdot 10^{-4}$
θ_{Hg}	0°	0°	—	40°	40°	$9.1 \cdot 10^{-3}$

Table 11a. Estimation of the Parameters (μ_b, σ_b, q_{bci}, λ_{bci}) of Test 3 (Code: LEV2)

Initial Values				Estimated Values			
μ_b (nm)	σ_b (nm)	q_{bci}	λ_{bci}	μ_b (nm)	σ_b (nm)	q_{bci}	λ_{bci}
60	30	0.245	3.06	60.0	30.0	0.238	2.962
60	30	0.245	3.06	67.2	46.9	0.317	3.06
30	40	0.0835	13.1	30.0	40.0	0.0821	12.74
30	40	0.0835	13.1	31.9	33.8	0.0806	9.493
45	60	0.1662	7.936	45.0	60.0	0.1631	5.36
45	60	0.1662	7.936	47.8	39.6	0.1657	3.8876

Table 11b. Estimation of the Parameters (μ_b, σ_b, q_{bc0}, λ_{bc0}, θ_{Hg}) of Test 3 (Code: LEV3)

Initial Values					Estimated Values				
μ_b (nm)	σ_b (nm)	q_{bc0}	λ_{bc0}	θ_{Hg}	μ_b (nm)	σ_b (nm)	q_{bc0}	λ_{bc0}	θ_{Hg}
60	30	0.35	5.0	40	60.0	30.0	0.403	5.05	40
60	30	0.39	6.0	40	61.5	44.2	0.39	6.72	40
30	40	0.15	16.0	40	30.0	40.0	0.117	20.09	40
30	40	0.15	15.0	40	36.2	34.1	0.15	13.58	40
45	60	0.22	7.0	40	45.0	60.0	0.2164	13.38	40
45	60	0.22	7.0	40	47.2	38.9	0.2428	9.18	39.9

Table 12. Estimation of the Parameters (μ_b, σ_b, q_{bci}, λ_{bci}, q_{bc0}, λ_{bc0}, θ_{Hg}) of Test 3 (Code: LEV23b)

Initial Values							Estimated Values							
μ_b (nm)	σ_b (nm)	q_{bci}	λ_{bci}	q_{bc0}	λ_{bc0}	θ_{Hg}	μ_b (nm)	σ_b (nm)	q_{bci}	λ_{bci}	q_{bc0}	λ_{bc0}	θ_{Hg}	SSR
60.0	30.0	0.238	2.96	0.405	5.05	40	62.7	44.6	0.287	3.666	0.403	6.606	40	$3.463 \cdot 10^{-4}$
64.3	45.5	0.317	3.06	0.39	6.72	40	52.7	41.0	0.207	4.75	0.2976	7.92	40	$9.675 \cdot 10^{-6}$
30.0	40.0	0.082	12.74	0.117	20.1	40	31.6	31.7	0.075	11.59	0.117	16.88	40	$3.75 \cdot 10^{-3}$
34.0	34.0	0.080	9.49	0.15	13.58	40	35.6	33.8	0.095	9.32	0.1451	13.98	40	$5.647 \cdot 10^{-5}$
45.0	60.0	0.163	5.36	0.216	13.4	40	44.1	37.6	0.1454	6.4	0.2164	10.04	40.2	$1.771 \cdot 10^{-5}$
47.5	39.3	0.166	3.88	0.243	9.2	40	47.6	39.1	0.1688	5.64	0.247	9.064	40	$2.719 \cdot 10^{-6}$

N_2 desorption curve for sample E (Figure 13a). The following picture of the pore structure of the two materials can be extracted from the parameter values of Table 15.

Sample D

- The sizes of throats ($\mu_b = 7.4$ nm) are clearly smaller than those of pores ($\mu_s = 18.1$ nm).
- Both the site ($\sigma_s/\mu_s = 0.1$) and bond ($\sigma_b/\mu_b = 0.39$) size distributions are narrow.
- The pores resemble capillaries ($\beta_s = 2.03$) of high angular porosity ($n_s = 3.02$).
- The pore network is multiply connected with high mean coordination number ($q_{bc0} = 0.0058$, $\lambda_{bc0} = 90.0$).

Sample E

- The sizes of throats ($\mu_b = 1.47$ nm) are smaller than those of pores ($\mu_s = 3.1$ nm).
- Both distributions are relatively narrow ($\sigma_b/\mu_b = 0.47$, $\sigma_s/\mu_s = 0.22$).
- The pores resemble capillaries ($\beta_s = 2.14$) of high angular porosity ($n_s = 3.0$).
- The pore network is well-connected ($q_{bc0} = 0.019$, $\lambda_{bc0} = 46.9$).

Comparatively, the pore network of sample D is similar to that of sample E, though the sizes of pores and throats in D are 5–6 times greater than those in E. These differences are also reflected in the value of the specific surface area, S_{BET} (Table 14) and are confirmed by TEM images (Figure 11a and 11b). Statistical properties of the geometrical characteristics of the 2-D features of pore cross sections of sample D were measured on TEM pictures (Figure 11a) by using the ScanPro 5.0 image analysis software. Given that in image analysis no distinction is made between pores and throats, the calculated Feret radius distribution of 2-D pore features ($\mu_F = 10.7$ nm, $\sigma_F = 6.6$ nm) was wider than the estimated pore radius distribution, and its mean value was in the range $\mu_b \leq \mu_F \leq \mu_s$. Furthermore, the shape factor of the pore cross sectionals ($\langle SF \rangle = 0.52$, $\sigma_{SF} = 0.15$) was close to but lower than that of equilateral triangles ($n_s = 3$, $SF = \pi\sqrt{3}/9$). Therefore, in the course of the geometrical model of polygonal pores, the irregular shape of pores of sample D (Figure 11a) might be better approximated by a value $n_s < 3$. Actually, the parameter estimation procedure led to a value $n_s \rightarrow 2$, but for reasons of geometrical inspection, the inequality $n_s \geq 3$ was set as a physical constraint.

Table 13. Comparison of True with Estimated Parameter Values of Test 3

Parameter	True Value	Estimated Value	Confidence Interval
μ_s (nm)	500	500	$2.1 \cdot 10^{-5}$
σ_s (nm)	300	300	$4.9 \cdot 10^{-5}$
n_s	4.0	4.0	$5.6 \cdot 10^{-7}$
β_s	2.0	2.0	$5.5 \cdot 10^{-9}$
μ_b (nm)	50	47.6	$2.4 \cdot 10^{-4}$
σ_b (nm)	40	39.1	0.022
q_{bci}	0.186	0.169	$4.4 \cdot 10^{-5}$
λ_{bci}	5.192	5.64	$1.9 \cdot 10^{-3}$
q_{bc0}	0.270	0.247	—
λ_{bc0}	8.479	9.064	$3.6 \cdot 10^{-3}$
θ_{Hg}	40	40	—

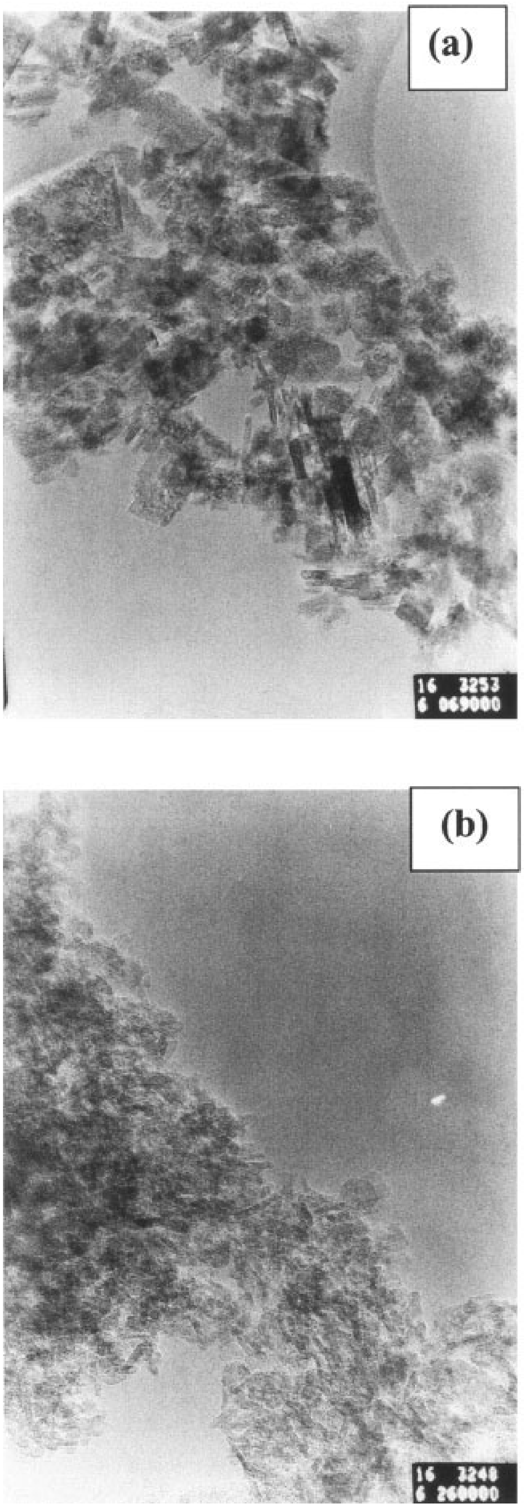

Figure 11. TEM images of (a) sample D (picture dimensions: 850 nm × 150 nm); (b) sample E (picture dimensions: 225 nm × 305 nm).

Initial guess of the total pore volume

For the majority of porous materials, the existence of meso- and macropores is reflected in incomplete N_2 adsorption/desorption curves, where a finite fraction of the pore volume is not filled with liquid N_2 at the maximum relative pressure (secondary desorption). Obviously, in all these cases, knowledge of the accurate V_p value is of crucial importance for the conversion of Hg injected and liquid N_2 adsorbed volumes to correct saturation values.

Table 14. Macroscopic Characteristics of Porous Materials

	N_2 Sorption		Hg Intrusion
Sample	V_{p,N_2} (cm^3/g)	S_{BET} (m^2/g)	$V_{p,Hg}$ (cm^3/g)
A	0.76	262	0.84
B	0.69	283	0.67
C	0.69	260	0.62
D	0.53	90	0.48
E	0.48	222	0.42

When attempting to match the secondary N_2 desorption curve to the Hg intrusion curve of a porous material, there is an ambiguity concerning the total pore volume, V_p. A method was developed to estimate the total pore volume, V_p, of a sample from the maximum Hg injected and N_2 absorbed volumes. Specifically, the total pore volume is considered equal to the sum of the Hg volume, V_{Hg} injected at the maximum capillary pressure P_{cf}, and the liquid N_2 volume, V_{LN2}, adsorbed at the relative pressure, x_h, specified by a relationship of the form

$$x_h = g[r_b(P_{cf})] \qquad (51)$$

where r_b is a common critical throat radius for Hg intrusion and N_2 desorption, respectively. However, uncertainties are always embedded into the calculated V_p value because of variations in sample porosity and experimental errors in volume measurements. Therefore, the relationship

$$V_p = V_{Hg}(P_{cf}) + V_{LN2}(x_h) \qquad (52)$$

provides a good initial guess rather than an accurate value of V_p. Alternatively, an initial guess of V_p can be obtained by summing the liquid N_2 volume adsorbed at the maximum relative pressure, x_f, and the mercury volume injected at the corresponding capillary pressure, P_{ch}.

Samples with secondary N_2 sorption isotherms

The methodology P2 (Figure 10) was used for the characterization of the pore structure of samples B and C, exhibiting

Table 15. Estimated Parameters for Samples D and E

	Sample D		Sample E	
Parameter	Estimated Value	Confidence Interval	Estimated Value	Confidence Interval
μ_s (nm)	18.2	0.23	3.1	0.04
σ_s (nm)	1.8	0.25	0.62	0.04
n_s	3.02	0.14	3.0	—
β_s	2.025	$7.5 \cdot 10^{-3}$	2.14	$6 \cdot 10^{-3}$
μ_b (nm)	7.4	0.67	1.47	0.02
σ_b (nm)	2.9	0.71	0.69	0.004
a_0	3.065	8.16	24.85	1.85
(q_{bc0})	(0.0058)		(0.0187)	
b_0	$1.74 \cdot 10^{-2}$	$3.6 \cdot 10^{-2}$	0.0805	—
(λ_{bc0})	(90.0)		(46.9)	

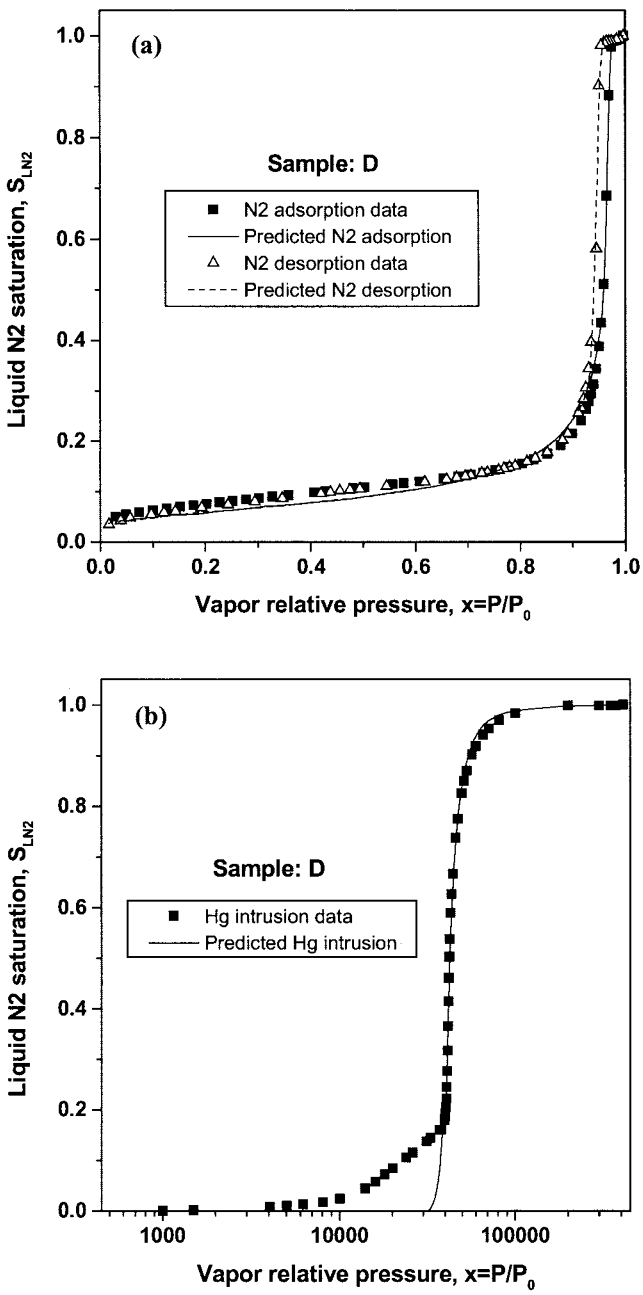

Figure 12. Model predictions (Table 15) vs. experimental data for sample D.

secondary N_2 desorption curves (Table 16). The prediction of the N_2 adsorption curve was improved significantly by using a bimodal pore-radius distribution consisting of two lognormal component distribution functions $f_{s1}(r;\ \mu_{s1},\ \sigma_{s1})$, $f_{s2}(r;\ \mu_{s2},\ \sigma_{s2})$ with contribution fractions, c_s and $(1 - c_s)$, respectively. The mean value, μ_s, and standard deviation, σ_s, are given by

$$\mu_s = c_s\mu_{s1} + (1 - c_s)\mu_{s2} \tag{53}$$

$$\mu_s^2 + \sigma_s^2 = c_s(\mu_{s1}^2 + \sigma_{s1}^2) + (1 - c_s)(\mu_{s2}^2 + \sigma_{s2}^2). \tag{54}$$

The mercury intrusion contact angle was kept constant (θ_{Hg} = 40°). An initial guess of the total pore volume, V_p (B: 0.813 cm^3/g, C: 0.833 cm^3/g) was obtained by using Eqs. 51 and 52. This parameter was kept constant in next steps, and included in the set of estimated parameters only in the final step of global optimization (code LEV123, Figure 10). The following picture can be deduced for the pore structure of samples B and C:

Sample B

- The mean aspect ratio of pore-to-throat radius is relatively low (μ_s/μ_b = 1.54).
- Both the pore- (σ_s/μ_s = 0.61) and throat- (σ_s/μ_s = 0.48) radius distributions are narrow.

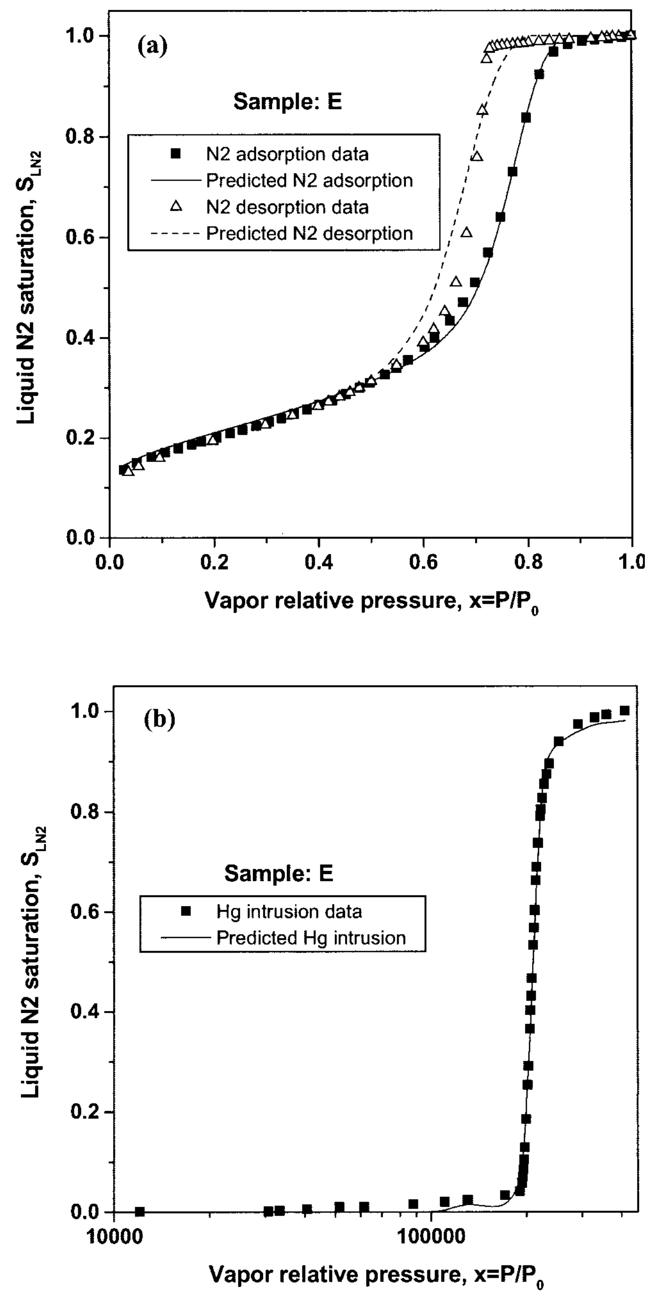

Figure 13. Model predictions (Table 15) vs. experimental data for sample E.

Table 16. Estimated Parameter Values for Samples B and C

	Sample B		Sample C	
Parameter	Estimated Value	Confidence Interval	Estimated Value	Confidence Interval
μ_{s1} (nm)	2.52	0.1	2.8	0.08
σ_{s1}/μ_{s1}	0.477	0.025	1.17	0.06
μ_{s2} (nm)	3.39	—	3.6	—
σ_{s2}/μ_{s2}	3.02	0.34	6.5	1.27
c_s	0.9906	0.0028	0.98	0.0065
μ_s	2.53		2.82	
σ_s	1.55		4.63	
n_s	3.0	—	3.0	—
β_s	2.16	0.0087	2.15	0.0066
μ_b (nm)	1.64	—	1.37	0.05
σ_b/μ_b	0.483	0.04	8.86	7.87
a_i	-0.9994	—	117.06	224.0
(q_{bci})	$(5.3 \cdot 10^{-4})$		(0.0724)	
b_i	$9.6 \cdot 10^{-5}$	$3 \cdot 10^{-5}$	0.427	0.0825
(λ_{bci})	(6.2)		(18.2)	
a_0	0.163	0.488	34.27	40.0
(q_{bc0})	(0.039)		(0.0803)	
b_0	0.0816	0.0275	0.386	—
(λ_{bc0})	(8.0)		(12.7)	
V_p (cm^3/g)	0.8	0.0168	0.7212	0.021

- The pore network is well connected ($q_{bc0} = 0.039$) and eventually *c–t* correlated ($\lambda_{bci} = 6.2$, $\lambda_{bc0} = 8.0$).

Sample C

- The mean aspect ratio of pore-to-throat radius is relatively low ($\mu_s/\mu_b = 2.05$).
- The pore-radius distribution is broad ($\sigma_s/\mu_s = 1.64$) and the throat-radius distribution is very broad ($\sigma_s/\mu_s = 8.86$).
- The pore network is clearly less well-connected than those of samples B, D, E ($q_{bc0} = 0.08$, $q_{bci} = 0.072$), whereas no strong *c–t* correlations are evident ($\lambda_{bci} = 18.2$, $\lambda_{bc0} = 12.7$).

In general, the experimental N_2 adsorption/desorption and Hg intrusion curves of samples B and C were reproduced satisfactorily by the models for the parameter values of Table 16 (Figures 14 and 15). The discrepancy observed between experiment and theoretical prediction over the high-pressure region of Hg intrusion curve for sample B (Figure 14b) is associated with inherent limitations of any simple geometrical pore model to represent precisely complex pore structures. For sample B, the relatively narrow throat-radius distribution and low percolation threshold (Table 16) are reflected in the abrupt filling of the pore network over a narrow pressure range, and the gradual filling of pore edges over higher pressures (Figure 14b). In order to overcome such inconsistencies, the geometrical pore model could be replaced by a statistical distribution of pore-shape factors. However, even then, the geometrical and topological properties produced would enable us to get a rough picture of a pore structure rather than an accurate map of the highly irregular pore space. For instance, the pore radius refers to an equivalent capillary radius rather than to a real geometrical dimension. On the other hand, the 3-D pore structure of a material can be modeled precisely by processing random 2-D images with stochastic methods of reconstruction (Liang et al., 2000). In order to be able to get more information concerning the detailed morphology of an irregular pore structure from the parameters of a simple or complex geometrical model, the methodology presented here could be calibrated with respect to simulated results from stochastically reconstructed porous media.

Compared to the results given by the classic method of analysis (tube-bundle model), the present methodology produces narrower pore- and throat-radius distributions with lower mean values (Table 17), and these differences are attributed to the following factors: (1) a significant fraction of porosity is assigned to pore cusps, the volume of which is excluded from the definition of the pore or throat "radius"; (2) the calculated pore-radius distribution refers to number of pores and $\beta_s > 0$, while the corresponding distribution, derived from the differentiation of the N_2 adsorption curve refers to pore volume; (3) the higher the percolation threshold q_{bc0} (C > B > E > D) the longer the distance of the conventionally calculated μ_b value from the currently estimated one (Table 17).

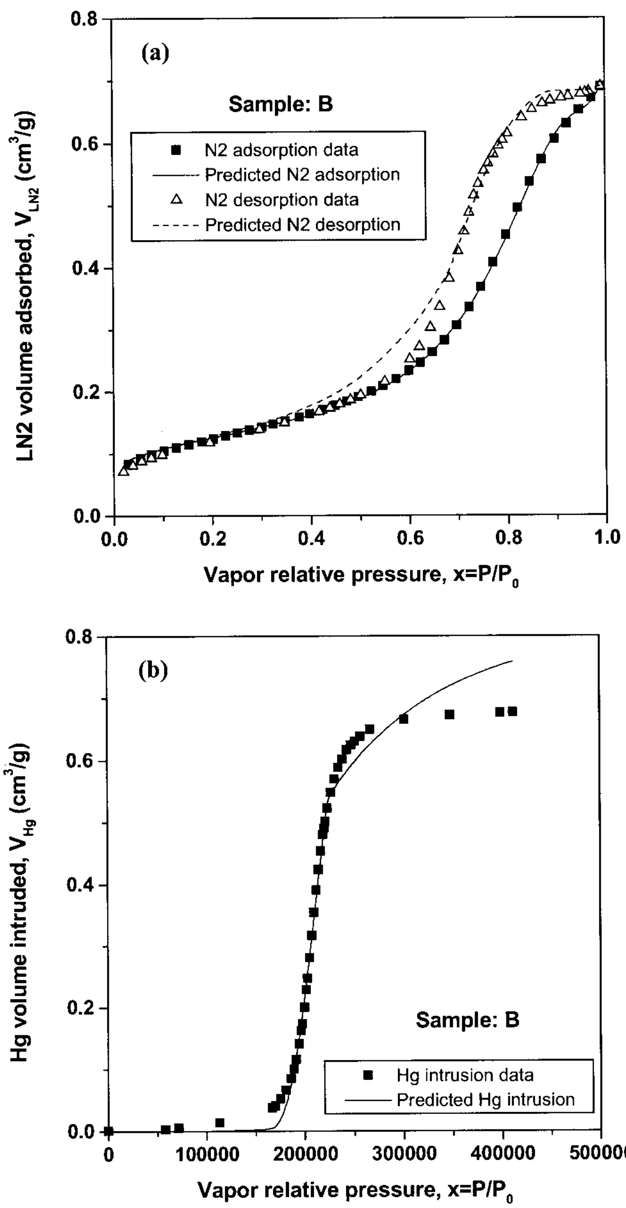

Figure 14. Model predictions (Table 16) vs. experimental data for sample B.

Finally, the numerical algorithms of parameter estimation could be improved and decoupled from *a priori* knowledge of the specific characteristics of the statistical properties of pore- and throat-size distributions (such as, unimodal, bimodal, log-normal) or the form of the accessibility function, if these properties were represented by general b-splines (Bard, 1974).

Conclusions

A methodology was developed for the determination of the geometrical and topological parameters of the pore structure of porous materials from experimental data of Hg porosimetry and N_2 adsorption/desorption. Mathematical models of the corresponding physical processes were integrated into numerical codes of nonlinear parameter estimation. The methodology comprises multistep procedures where the parameter values are updated successively and different data sets are used at each step. Specifically, two multistep procedures were developed for porous materials exhibiting complete (primary) and incomplete (secondary) N_2 sorption isotherms, respectively. These procedures were evaluated and calibrated with respect to "test" materials of well-known parameter values, and then were used to determine the structural properties of four samples of porous alumina.

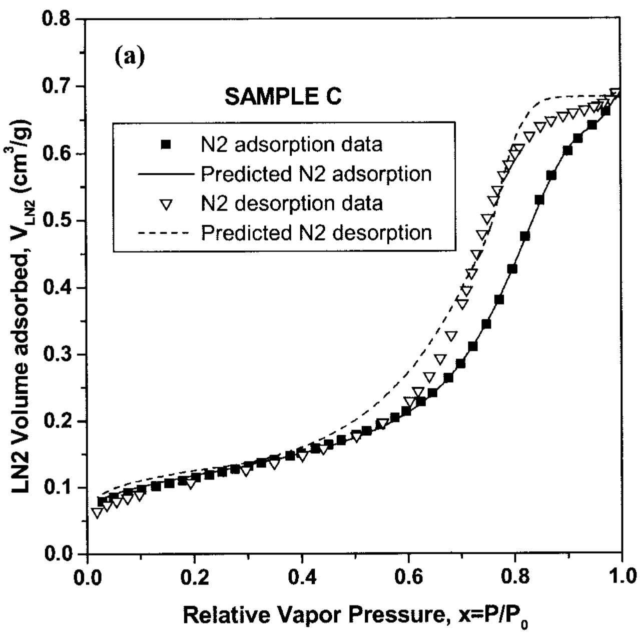

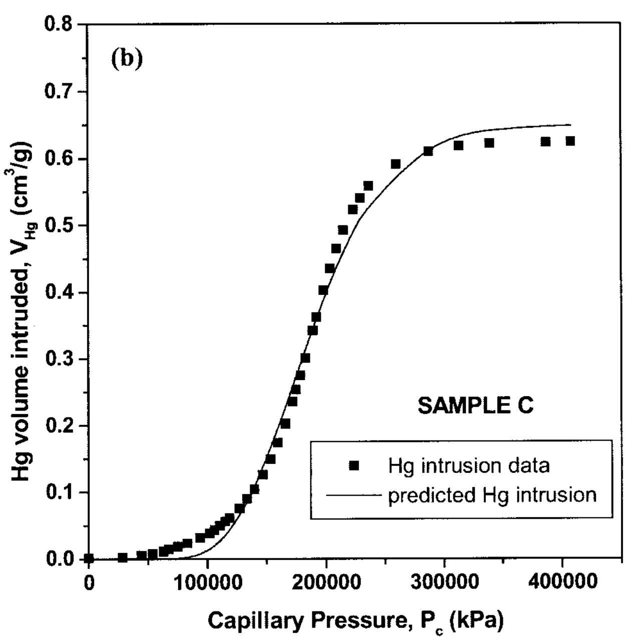

Figure 15. Model predictions (Table 16) vs. experimental data for sample C.

Table 17. Comparison of Estimated Parameter Values with Those Obtained from the Differentiation of N_2 Sorption and Hg Intrusion Curves

Method	μ_s (nm)	σ_s (nm)	μ_b (nm)	σ_b (nm)
Sample D				
N_2 sorption	24.0	17.4	16.4	14.2
Hg intrusion			22.1	33.0
Present method	18.2	1.8	7.4	2.9
Sample E				
N_2 sorption	4.5	17.4	3.8	13.0
Hg intrusion			3.6	1.9
Present method	3.1	0.62	1.47	0.69
Sample B				
N_2 sorption	7.13	10.8	4.3	6.8
Hg intrusion			8.9	112.4
Present method	2.53	1.55	1.64	0.8
Sample C				
N_2 sorption	8.1	12.9	5.3	9.9
Hg intrusion			7.9	90.7
Present method	2.82	4.63	1.37	12.14

Summary of the main conclusions

- Information concerning pore-network topology and spatial pore-size correlations can be deduced from accessibility functions; i these functions, along with pore- and throat-size distributions, can be estimated from N_2 sorption and Hg intrusion data.
- The critical step in the pore-structure analysis is the selection of good initial values for the parameters by employing properly experimental data and theoretical models.
- The following general rules are suggested for the estimation of reliable parameter values for the structure of mesoporous materials from Hg intrusion and N_2 adsorption/desorption curves:

(1) The pore-size distribution and pore-shape factors are estimated from N_2 adsorption data.

(2) The throat-size distribution and network accessibility function are estimated from N_2 desorption and Hg intrusion curve.

(3) Finally, the total pore volume per unit mass is estimated by using all data in a global optimization step.

- The parameter values obtained by using the present methodology for the analysis of the structure of porous alumina samples differ substantially from those provided by the conventional method of analysis.
- Accurate representation of the morphology of the pore structure of real materials can be obtained if the present meth-

odology is calibrated against well-characterized real materials, and/or 3-D stochastically reconstructed porous media.

Acknowledgments

This work was supported by Haldor Topsoe A/S (Contract No: 37013-170-5, 1/12/1999–30/11/2001) and by the Institute of Chemical Engineering and High Temperature Chemical Processes.

Notation

A = pore cross-sectional area
$A_{\rm eff}$ = pore cross-sectional area occupied by the nonwetting fluid
a_i, a_0 = proexponential factor involved in accessibility function
b = parameter involved in FHH equation
b_i, b_0 = exponent involved in secondary/primary accessibility function
c = lumped parameter of Kelvin equation
c_b, c_s = contribution fraction of the component distribution of large sizes, 1, to the total throat/pore size distribution
f_b, f_s = throat/pore size distribution function
F = fraction of pore cross-sectional area occupied by the wetting fluid
G = pore-shape factor
n_s = number of sides in a polygonal pore
P = pore perimeter
$P_{\rm eff}$ = length of the contact line of nonwetting fluid with wetting fluid and solid
P_c = capillary pressure
P_{cf} = maximum capillary pressure
P_{ch} = capillary pressure corresponding to the maximum relative vapor pressure
q_b, q_s = fraction of bonds/sites allowable to the nonwetting fluid
q_{bi}, q_{si} = fraction of bonds/sites allowable to the nonwetting fluid at the start of drainage
q_{bci}, q_{bc0} = bond percolation threshold in secondary/primary drainage
r = pore/throat radius
r_b, r_s = critical throat/pore radius
r_c = radius of curvature
r_d = critical radius of curvature for nonwetting fluid invasion (drainage) in a throat
r_i = critical radius of curvature for nonwetting fluid retraction (imbibition) from a pore
$r_{\rm con}$ = critical radius of curvature for nitrogen condensation in a pore
$r_{\rm evp}$ = critical radius of curvature for nitrogen evaporation from a throat
s = parameter involved in FHH equation
$S_{\rm Hg}$ = mercury saturation
$S_{\rm LN2}$ = liquid nitrogen saturation
S_{f1}, S_{f2} = wetting fluid (vacuum/liquid nitrogen) saturation in pore cusps
$\langle SF\rangle$ = mean value of the pore-shape factor
t_c = thickness of nitrogen adsorbed layer
V_s = pore volume
V_p = total pore volume per mass unit
$V_{\rm Hg}$ = mercury volume
$V_{\rm LN2}$ = liquid nitrogen volume
x = relative vapor pressure
x_f = maximum relative vapor pressure at the end of adsorption
x_h = relative vapor pressure corresponding to the maximum capillary pressure
Y_{si}, Y_{s0} = site accessibility function of secondary/primary drainage

Greek letters

β_s = pore volume exponent
γ_{Hg} = mercury surface tension
γ_{LG} = N_2 liquid/vapor interfacial tension
θ_{Hg} = mercury intrusion contact angle
θ_{LG} = N_2 liquid/vapor contact angle
λ_{bci}, λ_{bc0} = slope of the secondary/primary accessibility function at the percolation threshold
μ_b, μ_s = mean value of the throat/pore size distribution
μ_F = mean value of the Feret radius distribution
σ_b, σ_s = standard deviation of the throat/pore size distribution
σ_F = standard deviation of the Feret radius distribution
σ_{SF} = standard deviation of the pore-shape factor distribution
σ = diameter of nitrogen molecule
ω = angle of pore cusps

Abbreviations

WF = wetting fluid
NWF = nonwetting fluid
LN2 = liquid nitrogen
Hg = mercury
LG = liquid/vapor interface

Literature Cited

Bard, Y., *Nonlinear Parameter Estimation,* Academic Press, London (1974).
Bodor, E. E., J. Skalny, S. Brunauer, J. Hagymassy, and M. Yudenfreund, “Pore Structures of Hydrated Calcium Silicates and Portland Cements by Nitrogen Adsorption,” *J. Colloid Interface Sci.,* **34,** 560 (1970).
Broekhoff, J. C. P., and J. H. de Boer, “Studies on Pore Systems in Catalysts. IX. Calculation of Pore Distributions from the Adsorption Branch of Nitrogen Sorption Isotherms in the Case of Open Cylindrical Pores. B. Applications,” *J. Catal.,* **9,** 15 (1967).
Broekhoff, J. C. P., and J. H. de Boer, “Studies on Pore Systems in Catalysts. XIII. Pore Distributions from the Desorption Branch of Nitrogen Sorption Isotherms in the Case of Cylindrical Pores. B. Applications,” *J. Catal.,* **10,** 377 (1968).
Cebeci, O. Z., “The Intrusion of Conical and Spherical Pores in Mercury Intrusion Porosimetry,” *J. Colloid Interface Sci.,* **78,** 383 (1980).
Chatzis, I., and F. A. L. Dullien, “The Modeling of Mercury Porosimetry and the Relative Permeability of Mercury in Sandstones Using Percolation Theory,” *Int. Chem. Eng.,* **25,** 47 (1985).
De Wit, L. A., and J. J. F. Scholten, “Studies on Pore Structure of Adsorbents and Catalysts. III. Comparison of Pore Size Distributions Determined in Chrysotile and Zirconia Samples by Mercury Porosimetry and Nitrogen Capillary Condensation,” *J. Catal.,* **36,** 36 (1975).
Diaz, C. E., I. Chatzis, and F. A. L. Dullien, “Simulation of Capillary Pressure Curves Using Bond Correlated Site Percolation on a Simple Cubic Network,” *Transp. Porous Media* **2,** 215 (1987).
Everett, D. H., “Thermodynamics of Multiphase Fluids in Porous Media,” *J. Colloid Interface Sci.,* **52,** 189 (1975).
Everett, D. H., and J. M. Haynes, “Model Studies of Capillary Condensation. I. Cylindrical Pore Model with Zero Contact Angle,” *J. Colloid Interface Sci.,* **38,** 125 (1972).
Gladden, L. F., M. Hollewand, and P. Alexander, “Characterization of Structural Inhomogeneities in Porous Media,” *AIChE J.,* **41,** 894 (1995).
Gregg, S. J., and K. S. W. Sing, *Adsorption, Surface Area and Porosity,* Academic Press, London (1982).
Ioannidis, M. A., and I. Chatzis, “Network Modelling of Pore Structure and Transport Properties of Porous Media,” *Chem. Eng. Sci.,* **48,** 951 (1993).
Ioannidis, M. A., I. Chatzis, and E. A. Sudicky, “The Effect of Spatial Correlations on the Accessibility Characteristics of Three-Dimensional Cubic Networks as Related to Drainage Displacements in Porous Media,” *Water Resour. Res.,* **29,** 1777 (1993).
Jessop, C. A., S. M. Riddiford, N. A. Seaton, J. P. R. B. Walton, and N. Quirke, “The Determination of the Pore Size Distribution of Porous Solids Using a Molecular Model to Interpret Nitrogen Adsorption Measurements,” *Proceedings of the Third IUPAC Symposium on Characterization of Porous Solids COPS-II,* Rodriguez-Reinoso et al., eds., Elsevier, Amsterdam, p. 123 (1991).
Jonas, M., and J. R. Schopper, “The Radii Inversion Problem Associated with the Hg Capillary Pressure Experiment,” *Transp. Porous Media,* **14,** 33 (1994).
Lapidus, G. R., A. M. Lane, K. M. Ng, and W. C. Conner, “Interpretation of Mercury Porosimetry Data Using a Pore-Throat Network Model,” *Chem. Eng. Commun.,* **38,** 33 (1985).

Larson, R. G., and N. R. Morrow, "Effects of Sample Size on Capillary Pressures in Porous Media," *Powder Technol.,* **30,** 123 (1981).
Legait, B., "Laminar Flow of Two Phases Through a Capillary Tube with Variable Square Cross-Section," *J. Colloid Interface Sci.,* **96,** 28 (1983).
Li, Y., W. G. Laidlaw, and N. C. Wardlaw, "Sensitivity of Drainage and Imbibition to Pore Structures as Revealed by Computer Simulation of Displacement Process," *Adv. Colloid Interface Sci.,* **26,** 1 (1986).
Liang, Z., M. A. Ioannidis, and I. Chatzis, "Geometric and Topological Analysis of Three-Dimensional Porous Media: Pore Space Partitioning Based on Morphological Skeletonization," *J. Colloid Interface Sci.,* **221,** 13 (2000).
Liu, H., L. Zhang, and N. A. Seaton, "Determination of the Connectivity of Porous Solids from Nitrogen Sorption Measurements—II. Generalisation," *Chem. Eng. Sci.,* **47,** 4393 (1992).
Liu, H., L. Zhang, and N. A. Seaton, "Analysis of Sorption Hysteresis in Mesoporous Solids Using a Pore Network Model," *J. Coll. Int. Sci.,* **156,** 285 (1993).
Mason, G., "Model of the Pore Space in a Random Packing of Equal Spheres," *J. Colloid Interface Sci.,* **35,** 279 (1971).
Mason, G., "The Effect of Pore Space Connectivity on the Hysteresis of Capillary Condensation in Adsorption-Desorption Isotherms," *J. Colloid Interface Sci.,* **88,** 36 (1982).
Mason, G., "A Model of Adsorption-Desorption Hysteresis in which Hysteresis is Primarily Developed by the Interconnections in a Network of Pores," *Proc. Roy. Soc. London,* **A390,** 47 (1983).
Mason, G., "Determination of the Pore-Size Distributions and Pore Space Interconnectivity of Vycor Porous Glass from Adsorption-Desorption Hysteresis Capillary Condensation Isotherms," *Proc. Roy. Soc. London,* **A415,** 435 (1988).
Mason, G., and N. R. Morrow, "Capillary Behavior of a Perfectly Wetting Liquid in Irregular Triangular Tubes," *J. Colloid Interface Sci.,* **141,** 262 (1991).
Mason, G., and N. R. Morrow, "Effect of Contact Angle on Capillary Displacement Curvatures in Pore Throats Formed by Spheres," *J. Colloid Interface Sci.,* **168,** 130 (1994).
Matthews, G. P., A. K. Moss, and C. J. Ridgway, "The Effects of Correlated Networks on Mercury Intrusion Simulations and Permeabilities of Sandstone and Other Porous Media," *Powder Technol.,* **83,** 61 (1995).
Mayer, R. P., and R. A. Stowe, "Mercury Porosimetry—Breakthrough Pressure for Penetration Between Packed Spheres," *J. Colloid Sci.,* **20,** 893 (1965).
Mayer, R. P., and R. A. Stowe, "Mercury Porosimetry: Filling of Toroidal Void Volume Following Breakthrough Between Packed Spheres," *J. Phys. Chem.,* **70,** 3867 (1966).
Mishra, B. K., and M. M. Sharma, "Measurement of Pore Size Distributions from Capillary Pressure Curves," *AIChE J.,* **34,** 684 (1988).
Miyahara, M., T. Yoshioka, and M. Okazaki, "Observation of Interface Curvature of Capillary Condensed Phase in Slit-Shaped Nano Pore with a New MD Simulation Method," *Proceedings of the Fourth IUPAC Symposium on the Characterization of Porous Solids (COPS-IV),* B. McEnaney et al., eds., Royal Society of Chemistry, Cambridge, p. 413 (1997).
Moscou, L., and S. Lub, "Practical Use of Mercury Porosimetry in the Study of Porous Solids," *Powder Technol.,* **29,** 45 (1981).
Orr, F. M., L. E. Scriven, and A. P. Rivas, "Pendular Rings Between Solids: Meniscus Properties and Capillary Force," *J. Fluid Mech.,* **67,** 723 (1975).
Ransohoff, T. C., P. A. Gauglitz, and C. J. Radke, "Snap-Off of Gas Bubbles in Smoothly Constricted Noncircular Capillaries," *AIChE J.,* **33,** 753 (1987).
Renault, P., "Theoretical Studies of Mercury Intrusion in Some Networks: Testing the Applicability of Mercury Intrusion in the Size Characterisation of the Lacunar Pore Space of Soil Samples," *Transp. Porous Media,* **3,** 529 (1988).
Renault, P., "The Effect of Spatially Correlated Blocking-Up of Some Bonds or Nodes of a Network on the Percolation Threshold," *Transp. Porous Media,* **6,** 451 (1991).
Ridgway, C. J., and G. P. Matthews, "Modelling of Pore-Level Properties," *Proceedings of the Fourth IUPAC Symposium on the Characterization of Porous Solids (COPS-IV),* B. McEnaney et al., eds., Royal Society of Chemistry, Cambridge, p. 343 (1997).
Rigby, S. P., "A Hierarchical Structural Model for the Interpretation of Mercury Porosimetry and Nitrogen Sorption," *J. Colloid Interface Sci.,* **224,** 382 (2000).
Sahimi, M., "Flow Phenomena in Rocks: From Continuum Models to Fractals, Percolation, Cellular Automata and Simulated Annealing," *Rev. Mod. Phys.,* **65,** 1393 (1993).
Seaton, N. A., "Determination of the Connectivity of Porous Solids from Nitrogen Sorption Measurements," *Chem. Eng. Sci.,* **46,** 1895 (1991).
Smithwick, R. W., "A Generalized Analysis for Mercury Porosimetry," *Powder Technol.,* **33,** 201 (1982).
Spitzer, Z., "Mercury Porosimetry and Its Applications to the Analysis of Coal Pore Structure," *Powder Technol.,* **29,** 177 (1981).
Stauffer, D., and A. Aharony, *Introduction to Percolation Theory,* Taylor & Francis, London (1992).
Steele, W., and M. J. Bojan, "Computer Simulations of Sorption in Cylindrical Pores with Varying Pore-Wall Heterogeneity," *Proceedings of the Fourth IUPAC Symposium on the Characterization of Porous Solids (COPS-IV),* B. McEnaney et al., eds., Royal Society of Chemistry, Cambridge, p. 49 (1997).
Stewart, W. E., M. Caracotsios, and J. P. Sorensen, "Parameter Estimation from Multiresponse Data," *AIChE J.,* **38,** 641 (1992).
Stewart, W. E., T. L. Henson, and G. E. P. Box, "Model Discrimination and Criticism with Single-Response Data," *AIChE J.,* **42,** 3055 (1996).
Stewart, W. E., Y. Shon, and G. E. P. Box, "Discrimination and Goodness of Fit of Multiresponse Mechanistic Models," *AIChE J.,* **44,** 1404 (1998).
Tsakiroglou, C. D., and A. C. Payatakes, "A New Simulator of Mercury Porosimetry for the Characterization of Porous Materials," *J. Colloid Interface Sci.,* **137,** 315 (1990).
Tsakiroglou, C. D., and A. C. Payatakes, "Effects of Pore Size Correlations on Mercury Porosimetry Curves," *J. Colloid Interface Sci.,* **146,** 479 (1991a).
Tsakiroglou, C. D., and A. C. Payatakes, "A New Mercury Intrusion-Retraction Simulator Used as a Means for the Characterization of Porous Materials," *Proceedings of IUPAC-Symposium COPS-II,* F. Rodriguez-Reinoso et al., eds., Elsevier, Amsterdam, p. 169 (1991b).
Tsakiroglou, C. D., and A. C. Payatakes, "Pore-Wall Roughness as a Fractal Surface and Theoretical Simulation of Mercury Intrusion/Retraction in Porous Media," *J. Colloid Interface Sci.,* **159,** 287 (1993).
Tsakiroglou, C. D., G. B. Kolonis, T. C. Roumeliotis, and A. C. Payatakes, "Mercury Penetration and Snap-Off in Lenticular Pores," *J. Colloid Interface Sci.,* **193,** 259 (1997).
Tsakiroglou, C. D., and A. C. Payatakes, "Mercury Intrusion and Retraction in Model Porous Media," *Adv. Colloid Interface Sci.,* **75,** 215 (1998).
Tsakiroglou, C. D., and M. Fleury, "Pore Network Analysis of Resistivity Index for Water-Wet Porous Media," *Transp. Porous Media,* **35,** 89 (1999).
Tsakiroglou, C. D., and A. C. Payatakes, "Characterization of the Pore Structure of Reservoir Rocks with the Aid of Serial Sectioning Analysis, Mercury Porosimetry and Network Simulation," *Adv. Water Resour.,* **23,** 773 (2000).
Webb, P. A., and C. Orr, *Analytical Methods in Fine Particle Technology,* Micromeritics Instrument Corporation, Norcross, GA (1997).
Wong, H., S. Morris, and C. J. Radke, "Three-Dimensional Menisci in Polygonal Capillaries," *J. Colloid Interface Sci.,* **148,** 317 (1992).
Xu, K., J.-F. Daian, and D. Quenard, "Multiscale Structures to Describe Porous Media. Part I: Theoretical Background and Invasion by Fluids," *Transp. Porous Media,* **26,** 51 (1997).
Yanuka, M., "Percolation Processes and Porous Media. II. Computer Calculations of Percolation Probabilities and Cluster Formation," *J. Colloid Interface Sci.,* **127,** 35 (1989a).
Yanuka, M., "Percolation Processes and Porous Media. III. Prediction of the Capillary Hysteresis Loop from Geometrical and Topological Information of Pore Space," *J. Colloid Interface Sci.,* **127,** 48 (1989b).

Appendix

(1) At a relative pressure x_D the critical curvature radius of desorption, $r_{c,D}$ is given by

$$r_{c,D} = \frac{c}{\ln(1/x_D)} \tag{A1}$$

(2) The critical chamber size $r_{s,D}$ is given by

$$r_{s,D} = r_b = \frac{4FGr_{c,D}}{(\cos\theta_{LG} - \sqrt{\cos^2\theta_{LG} - 4FG})} + \sigma(b/c)^{1/s} r_{c,D}^{1/2} \quad \text{if} \quad r_b \le r_{si} \tag{A2}$$

$$r_{s,D} = r_{si} \qquad if \quad r_b > r_{si} \tag{A3}$$

(3) The critical curvature radius $r_{c,A}$ is obtained by

$$r_{s,A} = 4G[F + (\pi - n_s\theta_{LG})]r_{c,A} + \sigma(b/c)^{1/s} r_{c,A}^{1/s} \tag{A4}$$

where

$$r_{s,A} = r_{s,D} \tag{A5}$$

(4) The relative pressure of adsorption is given by

$$x_A = \exp(-c/r_{c,A}) \tag{A6}$$

(5) The accessibility function is approximated by the relationship

$$Y_{si} = q_s \frac{(q_s - q_{si})[1 - S_{LN2,D}(x_D)] + q_{si}\lfloor 1 - S'_{LN2,A}(x_A) \rfloor - q_s\varphi_{si}}{q_{si}[1 - S'_{LN2,A}(x_A)] + (q_s - q_{si})[1 - S_{LN2,A}(x_A)] - q_s\varphi_{si}} \tag{A7}$$

where $x_A \neq x_D$,

$$S'_{LN2,A}(x_A) = \frac{\int_0^{r_{s,A}} f_s(r)V_s(r)\,dr}{\int_0^\infty f_s(r)V_s(r)\,dr} \tag{A8}$$

$$\varphi_{si} = \frac{\int_{r_{si}}^\infty f_s(r)V_s(r)\,dr}{\int_0^\infty f_s(r)V_s(r)\,dr} \tag{A9}$$

$$q_{si} = \int_{r_{si}}^{\infty} f_s(r)\,dr \tag{A10}$$

(6) If the pore space is entirely occupied by liquid N_2 at the end of adsorption, that is, $q_{si} = \varphi_{si} = 0.0$, then Eq. 47 is simplified to

$$Y_{si} = q_s \frac{\lfloor 1 - S_{LN2,D}(x_D) \rfloor}{[1 - S_{LN2,A}(x_A)]} \tag{A11}$$

Equations 41–50 can be used in combination with experimental N_2 adsorption/desorption data and selected or estimated values of the geometrical parameters (μ_s, σ_s, n_s, β_s, μ_b, σ_b) to obtain numerical estimates for the parameters of $Y_{si}(q_b)$.

Manuscript received Nov. 28, 2002, and revision received June 9, 2003.